AIMS Materials Science, 3(3): 1022-1053.
DOI: 10.3934/matersci.2016.3.1022
Received: 15 March 2016
Accepted: 07 July 2016
Published: 26 July 2016

http://www.aimspress.com/journal/Materials

Short review

Process, structure, property and applications of metallic glasses

Bindusri Nair and B. Geetha Priyadarshini *

Nanotech Research Innovation and Incubation Centre, PSG Institute of Advanced Studies, Coimbatore, Tamil Nadu, India-641004

***** **Correspondence:** Email: bgp@psgias.ac.in.

Abstract: Metallic glasses (MGs) are gaining immense technological significance due to their unique structure-property relationship with renewed interest in diverse field of applications including biomedical implants, commercial products, machinery parts, and micro-electro-mechanical systems (MEMS). Various processing routes have been adopted to fabricate MGs with short-range ordering which is believed to be the genesis of unique structure. Understanding the structure of these unique materials is a long-standing unsolved mystery. Unlike crystalline counterpart, the outstanding properties of metallic glasses owing to the absence of grain boundaries is reported to exhibit high hardness, excellent strength, high elastic strain, and anti-corrosion properties. The combination of these remarkable properties would significantly contribute to improvement of performance and reliability of these materials when incorporated as bio-implants. The nucleation and growth of metallic glasses is driven by thermodynamics and kinetics in non-equilibrium conditions. This comprehensive review article discusses the various attributes of metallic glasses with an aim to understand the fundamentals of relationship process-structure-property existing in such unique class of material.

Keywords: metallic glasses; glass transition; amorphous; mechanical properties

1. Introduction

Metallic Glasses (MG) are a class of materials which has caught the eye of many researchers since Klement et al's [1] first work on Au-Si alloys in early 1960's. Owing to the amorphous nature MGs have interesting properties like high strength [2], wear and corrosion resistance [3], and biocompatibility [4]. However, early work on MGs was restricted to mainly binary alloy systems. All metallic glasses are classified into two categories viz: i) metal-metalloid glasses consisting of $M_{1-x}N_x$

where *x* is in the range 0.15–0.20, M is one or more of transition metals like Fe, Co, Ni, Pd, Au, and Pt and N is one or more of metalloids like P, B, Si, and C, ii) the metal-metal glasses which contain combinations of metals like Mg, Zn, Ca, Al, Cu, Ti, La and Ce [5]. Later, Inoue laid down the conditions for the formation of amorphous alloys: (i) should have more than three constituent elements, (ii) atomic size difference should be greater than 12%, (iii) must possess a negative heat of mixing, and (iv) alloy composition should be close to deep eutectics [6]. Structures of glassy alloy according to 3 component rule are seen to have short range icosahedral atomic arrangement [7].

Turnbull predicted that if a ratio, referred to as reduced glass transition temperature $T_{rg} = T_g/T_m$ where T_g is the glass transition temperature and T_m is the melting point temperature, is 2:3, the liquid becomes too sluggish and undercooled at relatively low cooling rates [8]. Certain multicomponent alloys like Zr-Al-Ni-Cu have good glass forming ability (GFA) which attributes to its amorphous nature (lack of long range periodicity) [9]. However, out of many factors affecting the glass forming ability, composition plays a major role, and variation in the composition can lead to changes in GFA of the alloys [10].

Heat conduction is slow in bulk metallic glasses as a result few compositions could only be produced in form of ribbons, foils, or wires so that heat could be extracted quickly enough to achieve the necessary cooling rate. Rapid quenching techniques like splat quenching [11] and melt spinning [12] are commonly used for processing and forming amorphous alloys in the form of ribbons. Later, other rapid solidification techniques from vapor or melt phase such as laser ablation and thermal spray deposition emerged [13]. Subsequently, a range of amorphous alloys were achieved by through solid-gas reaction [14], and solid-solid reaction [15]. Surface modification of metallic glasses was obtained by ion implantation and irradiation [16], electrodeposition [17] and mechanical alloying [18].

Intense research in MGs has led to the discovery of thin film metallic glasses (TFMGs) since the GFA can be further improved and wider composition ranges for amorphization can be obtained. As-deposited multi-component alloy thin films when annealed in supercooled liquid region ($\Delta T = T_x - T_g$, where T_x is the crystallization temperature and T_g is the glass transition temperature) found to be completely amorphous [19]. Remarkable properties are observed for thin film metallic glass with dramatic changes in the electrical and magnetic properties in ΔT range. For instance, Zr-based TFMG coating is shown to improve the substrate fatigue life by 30 times the bare Al alloy substrate [20]. Dramatic increase in resistivity for Cu-based TFMGs was observed from ~177 μΩ to ~4628 μΩ when annealed in ΔT range [21]. In case of Zr-Cu binary TFMG, Zr-rich composition showed a good corrosion resistance whereas the one with Cu-rich composition showed poor corrosion resistance depicting that the properties varies with composition [22]. It is only when they are annealed in super cooled liquid range, properties such as resistivity, strength, and elasticity was found to be improved. This can lead to a new class of materials which could find promising application in switches and actuators in MEMS devices [7]. Another class of interesting TFMG coatings composed of different multi-layered glasses is under current research which shows prospects for integrating into flexible devices. It was reported that the tensile strength of Cu foil supported amorphous/nanocrystalline ZrCu/Cu multilayered thin films were greater than those of monolithic Zr-Cu thin films [23].

This review in general discusses about the various process undertaken to obtain desirable structures of metallic glasses with enhanced structural and mechanical properties which are likely to find new avenues for diverse field of application. The commonly employed synthesis and processing

techniques for formation of metallic glasses has been classified as metallurgical and micro-technological processes. Post-fabrication process such as forming and surface modifications of bulk metallic glasses is discussed in brief. Thermodynamics and kinetics driven formation of metallic glasses is highlighted with an emphasis on structural behavior. Few important properties revealed by metallic glasses with relevant applications are presented. Finally, future prospects of these unique materials are highlighted.

2. Process

The processes followed for obtaining various forms of metallic glasses can be divided into two types *viz*: metallurgical processes and micro-technological processes.

2.1. Metallurgical Processes: Synthesis of Metallic glasses

These processes involve rapid formation of amorphous alloy resulting in the formation of amorphous alloys. The rate of cooling should be sufficiently rapid through the melting point such that it bypasses the crystal formation and directly reaches the glassy state. Casting method produces bulk metallic glasses, while spinning and quenching method produces metallic glass in the form of ribbons.

2.1.1. Mould Casting

Ingots of alloy were placed in a quartz crucible and melted using induction coils. They are then forced through an orifice at the bottom of quartz tube by argon gas pressure into a copper mould. The entire process is undertaken in Argon atmosphere inside a vacuum chamber [24]. Currently available mold casting techniques do not allow amorphous parts with complicated geometries. Stoica et al. reported inhibition of heterogeneous nucleation by modifying the surface tension of liquid alloy by applying a DC electrical current between molten metal and mould during ejection [25]. The surface tension when reduced molten alloy flows better, thus filling complicated moulds. The advantage of using this technique is that it is reproducible and scalable [26].

2.1.2. Centrifugal Mould Casting

The setup consists of a vacuum chamber in which a horizontal beam mounted on a vertical rod. One end of the beam is a vacuum box where graphite crucible is placed which is surrounded by a quartz tube and water cooled copper mould. The nozzle of the graphite crucible is aligned to the cavity of the copper mould. The melting is done by the induction coil surrounding the quartz tube. Once the melting is over the rod is rotated at 500 rpm speed which gives a centrifugal force to the melt. The crucible design is such that the vertical component of the centrifugal force drives the melt to the nozzle and due to the horizontal component the melt is forced into the mould cavity [27]. Metallic glasses $Fe_{72}B_{20}Si_4Nb_4$, $Fe_{36}Co_{36}B_{19}Si_5Nb_4$, $Fe_{43}Co_{14}Ni_{14}B_{20}Si_5Nb_4$ were casted in the form of rings by centrifugal mould casting.

2.1.3. Suction Casting

Suction casting employs an evacuation of the system to high vacuum to avoid oxidation of the alloy and the pressure difference between chambers integrated with the system leads to suction of an alloy melt which is arc-melted in an argon atmosphere onto a copper mould (water cooled) which is subjected to vibration [28]. The vibratory motion of the arc-melted metal results in a reduction of thermal contact between the specimen and the mould restricting the grain growth. Further, to reduce the likelihood of grain nucleation, the thermal isolation on the copper mould is provided to maintain large temperature difference between the molten metal and the cooled mould leading to higher cooling rate. Figueroa et al. produced Cu-Hf-Ti bulk metallic glass by suction casting within the argon arc furnace [29]. The advantage of this technique is that the metallic glass in the form of tubes and rods of a variable diameter can be processed.

2.1.4. Cold Rolling

Cold–rolling is one kind of solid state amorphization technique which leads to formation of metallic glasses in the form of sheets. The thickness of sheets can be as low as 0.8 mm with width and length can reach several centimeters. Accumulative Roll Bonding (ARB) is regarded as one of the severe plastic deformation processes. During ARB process, roll bonding, cutting, surface treatment, and stacking of the sheets are repeated to produce ultra-high plastic strain. ARB can be used to fabricate bulk non-equilibrium materials such as super saturated solid solution and metallic glass. Comparing with other mechanically alloying methods like ball milling, ARB can avoid contamination and temperature rise during the process.

Alternatively aligned pure Cu and Zr sheets were mechanically alloyed after imposing large plastic strain through ARB [30]. Thereafter, immediately followed by water quenching ARB processed samples were annealed for thermally driven amorphization. The Cu and Zr sheets were degreased and wire brushed followed by stacking. Thus stacked sheets were roll bonded with reduction in thickness by 75%. These stacked sheets were cut into four parts, degreased wire brushed stacked and then roll bonded. This ARB process was repeated for 10 cycles. Subjected to thermally driven amorphization takes place once the 10 cycle samples were annealed at 673 K for 30 min. The intrinsic plasticity of $Zr_{44}Ti_{11}Cu_{9.8}Ni_{10.2}Be_{25}$ and $Zr_{55}Ti_5Al_{10}Cu_{20}Ni_{10}$ are improved due to microstructural in-homogeneities upon cold rolling which are otherwise brittle [31]. The strong glass upon cold rolling is transformed to fragile glass and the change in viscosity (η) after rolling was due to local heating and the rise in Poisson's ratio (ν) was attributed to a non-Arrhenius liquid behavior [31].

Rizzi et al. reported cold rolling of $Al_{87}Ni_7La_6$ performed on ribbons embedded in pure Al foils and ribbons for studying deformation under constraint. The plastic deformation caused was measured by increase in length [32]. Cold rolled $Zr_{55}Cu_{30}Ni_5Al_{10}$ BMGs showed volume dilation across the entire range of thickness reduction fractions [33].

2.1.5. Splat Quenching

The formation of the first metallic glass of $Au_{75}Si_{25}$ was done by splat quenching technique wherein a gaseous shock wave atomizes the molten metal into droplets (~10 mg) which is then forced against a Cu chill block to form thin foils called splats [1]. Through this method, the molten

metal can be subjected to cooling rates in excess of 105–106 K/s. Subsequently, the nucleation and growth of crystalline phase is kinetically bypassed to achieve a frozen liquid configuration. Following this technique, various other quenching techniques were brought into practice. Later, Pd-Cu-Si, $Fe_{40}Ni_{40}B_{20}$ was formed by splat quenching [34]. Figure 1 shows a sketch of splat quenching apparatus where molten droplet is levitated in high frequency coils and by switching off the AC current the droplet falls on the cooling apparatus forming splats.

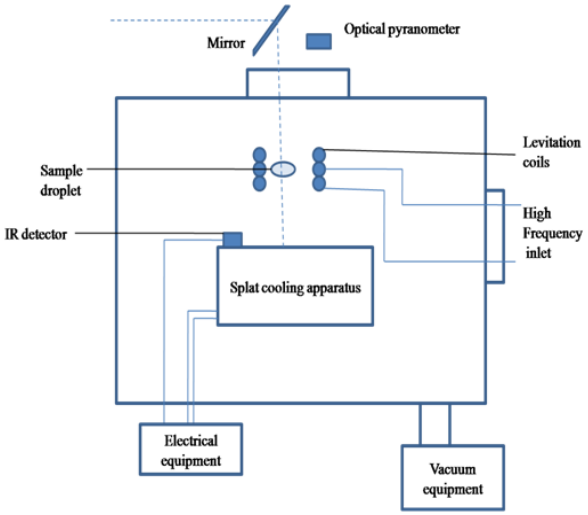

Figure 1. Sketch of splat cooling device.

2.1.6. Melt Spinning

Melt spinning is popular technique for making ribbon which uses molten material to flow from the nozzle in the form of a jet, which when comes in contact with rotating discs forms a melt puddle. Because of the low viscosity of the molten alloy, the shear layers extend only a few microns from the surface of the roller into the puddle and it stays on the roller surface. Due to the large temperature difference at the melt-substrate interface, the melt underneath the puddle solidifies into ribbon. The ribbon remains in contact with the disc surface until 10 °arc and then leaves it under the action of the centrifugal force as shown in Figure 2 [35]. Fe-Ni-P-B was the first metallic glassy ribbon exploited commercially for use in transformer core due to its soft magnetic property, leading to low-core losses. Xu et al. [36] reported the preparation of 5 alloys ($Zr_2Cu_{(1-x)}Pd_x$ x = 0.00, 0.25, 0.50, 0.75, 1.00) prepared by arc melting mixtures of high pure metals Zr (99.99 %), Pd (99.97%), Cu (99.99 %) in an ultra high purity Ar atmosphere. The alloy melt were spun at a wheel speed of 25 m/s and a constant pressure of 1.6×10^4 Pa in an ultra high purity He atmosphere. An increasing icosahedral short range order was observed in as-quenched alloy with increasing Pd.

Depending upon the cooling rate which is related to the circumferential velocity of the copper roller the structure obtained seemed to vary. Nanocrystal reinforced $Hf_{60}Ti_{15}Ni_{15}Cu_{10}$ was prepared by melt spinning at different spinning rates (25, 30 and 35 m/s) leading to a mixed structure of nanoscale icosahedral quasicrystalline (I phase), crystal (mainly α Hf/Ti) and glass phase [37]. At circumferential velocity of 40 m/s a single phase is formed. Hardness increases with decreasing

cooling rate *i.e.* circumferential velocity of Cu roller. The existence of icosahedral atomic clusters in melt contributes to the high glass forming ability and high thermal stability against crystallization [37].

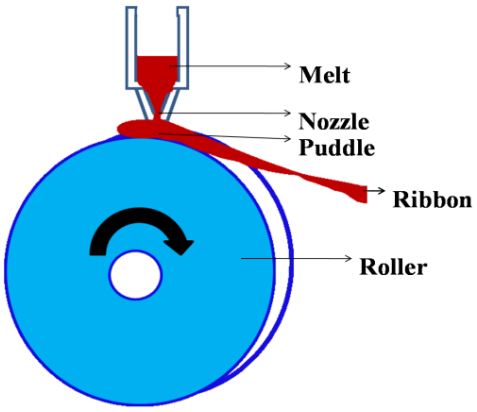

Figure 2. Schematic diagram of melt spinning technique.

2.2. Micro Technological Processes

These processes involve the fabrication of metallic glass alloys in the form of thin films; physical vapor deposition (PVD) including sputtering and evaporation. Due to rapid quenching rate, these processes leads to the formation of amorphous alloys thin films with ease and different composition of the alloys can be processed.

2.2.1. Sputter Deposition

Ye et al. performed a RF sputtering using the same target but different at wt% of $Zr_{53}Cu_{29}Al_{12}Ni_6$ was deposited on the silicon (100) substrate [39]. Due to the magnet placed below the target the plasma remains closer to the target than the substrate and thus the substrate remains unattacked by the plasma thus avoiding impurities. Under fast Fourier transform filtering of TEM image, the transition region between sputtered amorphous TFMG and the crystalline Si layer was observed.

Recently, as-formed bulk metallic glass ZrCuNiAl was chosen as the target and direct current was used for sputtering [40]. During sputtering Argon ions are bombarded towards the ZrCuNiAl bulk metallic glass target to remove surface atomic species which were then deposited on a 304 stainless steel substrate to form a ZrCuNiAl thin film which revealed greater adhesion with increase in sputtering power [40]. Conventionally, sputter deposition is used for processing of thin film metallic glasses with single alloy target or multiple elemental targets. However, co-sputtering using multi-target carousal oblique angle deposition (multi-COAD) was employed to fabricate nanostructures of $Zr_{44}Cu_{35}Al_{21}$ metallic glass. Hybrid nanostructures of ZrCuAl/NiNbSn were grown on 100 nm gold seeding particle. With multi-COAD the vapour chemistry was varied from ZrCuAl to NiNbSn when template is reoriented around its normal [41].

2.2.2. Pulsed Laser Deposition

Pulsed laser deposition (PLD) is ideal for the formation of thin films with complex compositions as the evaporation (congruent evaporation) is such that the composition of the target material is reflected on the thin film grown [42,43,44]. Here, photon energy is transferred to the bulk which is used to ablate the surface region into plasma. This plasma is then deposited on a substrate to form a thin film. Quality of the thin film formed is affected by various parameters like substrate temperature, ambient gas pressure of chamber and substrate target distance. Ag-Cu metallic glass was deposited on Ni foam by PLD technique for application in zinc-air batteries [43].

$Ti_{64}Cu_{12}Zr_{11}Co_5$ (Mo, Nb) was deposited by PLD technique on 316L stainless steel [45]. Optimum amorphicity was achieved at laser power 8 W. Mechanical properties and structure of $Ti_{64}Cu_{12}Zr_{11}Co_5$ (Mo, Nb) was controlled by varying laser parameters like wavelength and pulse duration. $Zr_{59}Ti_3Cu_{20}Al_{10}Ni_8$ was deposited on 304L stainless steel and its corrosion behavior was studied [46]. 'Donut' shaped features form due to short distances between substrate and target. These features occur (not frequently) when the molten droplet hits the substrate surface, rolls out and expands.

2.2.3. Evaporation

Thermal evaporation and electron beam evaporation processes are also employed for TFMG production. Thermal evaporation is one of the evaporation methods. It consists of sample holder, which is a container with a small orifice (Knudsen cell). In this orifice the solid comes to quasi-equilibrium with its vapour. To raise the vapour pressure of a target material, a DC current is passed through an electric resistance heater such that the target melts and its vapour pressure is increased to a useful range. The particles of the material escape the cell and arrive at the substrate and form a solid layer [47]. Pookat et al. reported CoFe based ultra thin films were prepared from a composite target by employing thermal evaporation [48]. These films were coated on naturally oxidized silicon substrate by thermal evaporation from a composite target having composition of $Co_{75}Fe_{14}Ni_4Si_5B_2$. Metglass2826 amorphous magnetic thin films were coated using thermal evaporation technique for applications in magnetostrictive sensor devices [49].

2.2.4. Annealing induced Amorphisation

Certain combination of thin film metallic glass alloys do not show amorphous nature, for instance $Zr_{31}Cu_{13}Al_9Ni$ as-sputtered films are crystalline at room temperature. These films are subjected to annealing in the supercooled liquid region turn into completely amorphous state [50]. Similarly, $Cu_{51}Zr_{42}Al_4Ti_3$ is a glass forming film on Si substrate showing an annealing induced amorphization [51]. It is seen that full amorphisation of $Cu_{51}Zr_{42}Al_4Ti_3$ takes place at 438 ℃ (which is in the supercooled liquid region) as shown in Figure 3. It is proposed that in addition to thermodynamic factor, the high interfacial energy arising from the nanocrystalline/amorphous interfaces are kinetically favourable for amorphisation. However, the supercooled liquid region is not a special feature of thin film metallic glass; it is also found in bulk metallic glasses. Based on the annealing temperature and annealing time both bulk and thin film metallic glass remains amorphous.

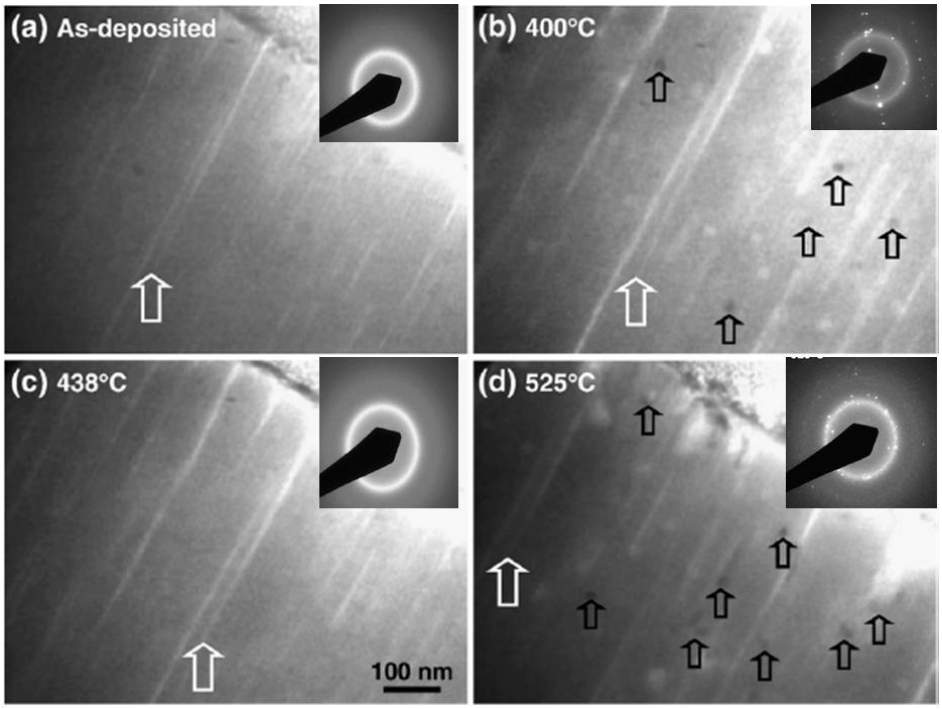

Figure 3. In situ TEM video image frames of film taken at: (a) as deposited (b) 400 ℃ (c) 438 ℃ (d) 525 ℃ indicating the crystalline phases and inset shows in situ TEM diffraction patterns of film taken at the corresponding temperatures. Major diffraction spots in (b) are indexed to be the $Cu_{10}Zr_7$ phase, while those in (d) are from $Cu_{10}Zr_7$ and $AlZr_2$ [51].

2.3. Other Fabrication Techniques

Fabrication of complex three-dimensional geometries of metallic glass for high-resolution surface textures or patterns can be attained for super cooled liquid temperatures where metallic glasses undergo drastic softening (super-plasticity). Surface modification of amorphous alloys can change the surface chemistry leading to nano-rough surfaces which often shows very good functional properties.

2.3.1. Thermoplastic Forming

In the supercooled liquid region the amorphous BMG first relaxes into a viscous liquid before it crystallizes. Thus, metallic glass in its supercooled liquid state can be processes under pressures and temperatures similar to those used for plastics with several minutes of processing time allowed before crystallization. The thermoplastic forming is carried out by reheating the BMG to its supercooled liquid region and relatively small forming pressure is sufficient to fill in the smallest features avoiding crystallization. Thermoplastic forming into a mould cavity results in precise replication of micro-features which are connected to large reservoir of amorphous material. For microelectromechanical systems (MEMS) and microstructure fabrication, this reservoir is separated from the parts using scrapers in a hot separation technique (in supercooled liquid region). Zr-based BMGs are fabricated using thermoplastic forming for MEMS application [38].

2.3.2. Laser Ablation

In laser ablation process short pulses of laser are preferred to long pulse lasers to avoid crystallization [52]. Ultrashort pulses (fs or ps) of laser can be used as they preserve the amorphous nature of metallic glasses after laser ablation. The irradiation time during a single pulse is shorter than electron cooling and lattice heating times, which prevents accumulation of heat and thus suppressing microstructural changes. Hsuan-Kai et al. [52] performed laser micromachining on Mg-Cu-Gd BMG using ultraviolet (UV) and infrared (IR) laser. It was found that higher micromachining rate was obtained using UV laser than IR laser, due to better absorption rate of UV by the Mg-Cu-Gd BMG and a higher photon energy.

Williams et al. [53] studied the interaction between a nanosecond laser pulse with a wavelength of 1064 nm and surface of $Zr_{41.2}Ti_{13.8}Cu_{12.5}Ni_{10}Be_{22.5}$ (Vitreloy 1). They reported formation of craters during irradiation, whose dimensions (diameter and depth) increased with augmentation of fluence for pulse length of 25 ns, 55 ns, 85 ns, and 140 ns. The cause for increased ablation was attributed to the fact that with increase of fluence for a given pulse length, the electrons within the subsystem of the material, transfer a high amount of energy to lattice. This caused a deeper penetration of the melt front into the workpiece, leading to increased material removal.

2.3.3. Plasma Immersed Ion Implantation (PIII)

Surface modification of BMGs is required to be done for avoiding environmental attack while in practical use. PIII is a fast and cost effective method which can be used for modifying surface properties by controlling the ion energy. During PIII surface absorption and implantation, diffusion takes place simultaneously on the surface with a non-line of sight characteristic mode. Abrupt interface and film delamination is much less observed for an ion implanted surface when compared to coating. Plasma treated surface has been shown to enhance the hardness and wear resistance of other materials without degrading the corrosion resistance. The influences of nitrogen and argon pulsed ion implantation with implantation voltages of 40 kV on $(Cu_{50}Zr_{50})_{92}Al_8$ BMG were investigated by Cheung and Shek [54]. PIII of as cast $(Cu_{50}Zr_{50})_{92}Al_8$ BMG samples were performed with radio-frequency by inductively coupled plasma immersion ion implanter. The frequency and pulse width were 30 μs and 200 Hz, respectively. ΔT_x (super cooled liquid region) and ΔH enthalpy of crystallization of as cast and implanted samples remains same indicating that amorphous nature of sample is preserved after PIII treatment under appropriate conditions. Huang in 2014 reported nitrogen PIII on $Zr_{62.5}Cu_{22.5}Fe_5Al_{10}$, which showed improved corrosion resistance after nitrogen implantation in simulated biological environment [55]. Tam and Shek in 2007 also reported nitrogen ion implantation by PIII on $Cu_{60}Zr_{30}Ti_{10}$ and it was observed that surface structure and composition changed in ion implanted BMG when compared to as cast BMG. The oxidation resistance was also improved by this surface modification process [56].

2.3.4. Electrodeposition

Sheng-Bao studied electro deposition on BMGs by electrodepositing fine grained copper on Zr-based BMG ($Zr_{41}Ti_{14}Cu_{12.5}Ni_{10}Be_{22.5}$) as substrate [57]. Copper was taken as anode and BMG was taken as the cathode as shown in Figure 4 and electrolyte consists of 200 g/L $CuSO_4$ and 60g/L

H_2SO_4. Different thickness of the coating was obtained by varying the electrodeposition time which showed a polycrystalline phase. Under the effect of copper coatings the ability of shear bands formation can be enhanced and eventually plasticity of the BMG can be improved. $Zr_{52.5}Cu_{17.9}Ni_{14.6}Al_{10}Ti_5$ BMG was electrodeposited with Ni film. The plasticity of the BMG was seen to improve once coated with Ni film [58].

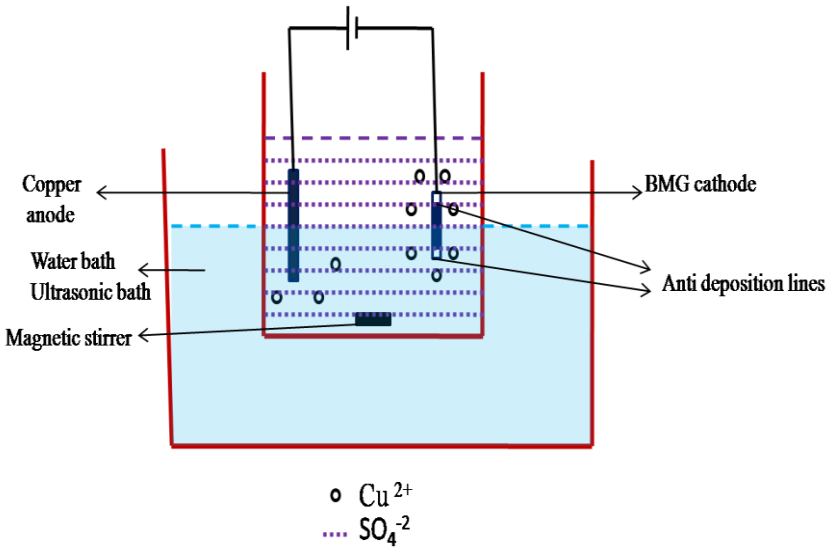

Figure 4. The schematic representation of electrodeposition set up.

3. Thermodynamic View of Glass Forming Ability

Metallic glass is not a thermodynamically stable state (excited state) and which eventually relax and transform to crystalline state (ground state) depending upon the temperature and time. Turnbull [59] reported that the metallic liquids can be significantly under cooled for extended time periods of time without undergoing crystallization process. Therefore, the glass becomes more stable when the free energy of the glassy phase (G_l) is lower than that of competing crystalline phase (G_s). In other words the gibbs free energy difference between liquid and crystal ($\Delta G_{l\text{-}s}$) indicates the driving force for crystallization. For the system with large number of alloy constituents, entropy increases due to high random packing of atoms which in turn lowers the change in free energy.

The reduced glass transition temperature (T_{rg}) i.e. the ratio of glass transition temperature (T_g) to liquidus temperature (T_l) is an indicator for glass forming ability of the alloy system. Inoue et al. proposed the supercooled liquid region ΔT (= $T_x - T_g$) where T_x is the onset of crystallization temperature of the glass to measure glass forming ability (GFA) [60]. Lu and Liu showed that the GFA parameter γ (= $T_x/T_l + T_g$) is a strong parameter to predict GFA [61]. Based on thermodynamic analysis mainly Gibbs free energy difference between liquid and crystal a new parameter was proposed by Ji Xiu-lin and Pan Ye (figure 5) [62]. The expression given by Thompson and Spaepen [63] is important in describing the $\Delta G_{l\text{-}s}$:

$$\Delta G_{l-s} = \frac{2\Delta H_m T(T_m - T)}{T_m(T_m + T)} \qquad (1)$$

where T_m is the melting temperature, ΔH_m is the enthalpy of fusion and T is the temperature of the supercooled liquid. In supercooled alloying liquids, lower the $\Delta G_{l\text{-}s}$, the more stable and better the GFA of the liquid. GFA is related to $\Delta G_{l\text{-}s}$ by following relationship:

$$GFA\alpha \frac{1}{(\Delta G_{l-s})} \alpha \frac{T_m(T_m+T)}{\Delta H_m T(T_m-T)} \quad (2)$$

At slower cooling rates, the glass freezes at lower temperature, whereas at higher cooling rates it undergoes structural relaxation readily at lower temperature. It is reported that the T_g detected from differential scanning calorimetry is different from the actual freezing temperature of a metallic glass. But the above expression of $\Delta G_{l\text{-}s}$ is derived from the continuous cooling process. Therefore the GFA parameter directly using Equation (2) has no good correlation with GFA. For glass transition of an alloying system, two equilibrium states, amorphous and liquid states are emphasized. From the viewpoint of heating process, the glass is still in amorphous state before system temperature exceeds T_g and the alloying system is not in a real liquid state before it reaches T_l. So, T_x and T_l are thermal stability gauges of the glass and the liquid respectively [64]. Thus, T_m is replaced by T_l (the temperature of a liquid state) and T is replaced by T_x (the temperature of an amorphous state). Therefore, new GFA parameter (ω) is in inversely proportion to Gibbs free energy difference of the alloying system from T_l to T_x and the following expression can be obtained from Equation (2):

$$\omega = \frac{T_l(T_l+T_X)}{T_X(T_l-T_X)} \quad (3)$$

From Equation 3, ω is a function of α (= T_x/T_l) and a shows positive correlation. ω has the accordant trends of GFA description with α and also expands the difference of values between descriptive parameters. Ji and Pan applied this new parameter *ω* to estimate the GFA of Cu-Ag-Zr-Ti and Cu-Zr-Ti-Al BMGs and the results obtained were consistent with experimental results [62].

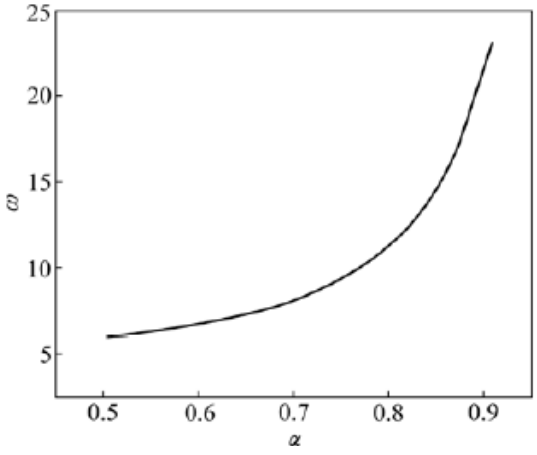

Figure 5. Function relationship between GFA parameters ω and α [62].

4. Glass Transition Kinetics

As the amorphous matrix changes from glassy state to molten state in glass transition region there is a change in heat capacity which is accompanied by absorption of heat. Therefore, the glass formation could be achieved if the liquid is cooled rapidly to prevent the formation of a crystalline

phase. Thus, the formation of glassy state seems to govern by purely kinetics. The glass transition activation energy (E) is the amount of energy required to jump from one metastable state to another. Activation energy of thermal relaxation of metallic glasses can be determined by using the theory of glass transition kinetics and structural relaxation (transformation from perturbed state to ground state) from heating rate, *β*, dependence of glass transition temperature as developed by Moynihan and others which was reported by Ashmi et al. [65]:

$$\frac{d \ln \beta}{d \ln(\frac{1}{T_g})} = -\frac{E}{R} \quad (4)$$

β is the heating rate and R is universal gas constant. Another method to find out activation energy of glass transition is the Kissinger method and its equation is:

$$\frac{d \ln \frac{\beta}{T_g^2}}{d \ln(\frac{1}{T_g})} = -\frac{E}{R} \quad (5)$$

It is also known that GFA is also a complex function of fragility which is defined as the increasing rate of viscosity of an undercooled liquid at a glass transition temperature in the cooling process. The fragility index *m*, which is a measure of the rate at which the relaxation time decreases with increasing temperature around T_g and is given by [66].

$$m = \frac{E}{RT_g \ln 10} \quad (6)$$

According to the value of fragility index, *m*, glass forming liquid can be categorized into strong glass former and fragile liquid. If the fragility index < 16 the system is a strong glass former, whereas if m is between 16 to 200 system is fragile. For $Co_{66}Si_{12}B_{16}Fe_4Mo_2$ metallic glass the fragility index is < 16 when measured by both Moynihan's method and Kissinger's equation which is 9.33 and 8.48 respectively for a heating rate of 10 ℃/min.

Strong glass formers show very little change in their equilibrium viscosity or relaxation time as glass transition temperature is approached whereas fragile glass formers show much variation in viscosities with temperature. The excellent glass former $Zr_{41.2}Ti_{13.8}Cu_{12.5}Ni_{10}Be_{22.5}$ with *m* exceeding 20, can be considered as a kinetically stabilized alloy [67]. Considering, $Pt_{57.3}Cu_{14.6}Ni_{5.3}P_{22.8}$, with a *m* of 16.4, has less exceptional kinetic properties.

Transformation to a glass does not take place at one strictly defined temperature, but occurs within a temperature range, known as the transformation region. For $Co_{66}Si_{12}B_{16}Fe_4Mo_2$ system the glass transition temperature increases with increase in heating rate as there is less time for initiation of nuclei formation and growth. Hence, T_g shifts towards higher values as heating rates increases.

5. Structure of Metallic Glasses

A structural model that brings together the features of randomness, short range forces, and medium range forces was studied by Daniel et al. [68]. These three are found to co-exist in metallic glasses. In this structure the short range order exists as a solute centered atomic clusters which also

include the icosahedral structure. The short range icosahedral order is preferred and favoured by solvent-centered clusters too. Medium range order is driven by solute-solute avoidance which results from the organization in space of overlapping, percolating via connected pathways and quasi equivalent clusters. Cubic like and icosahedral organization of these clusters are consistent with measured medium range order. Microscopic free volume in the efficient cluster packing model is able to represent experimental and computational results, showing free volume complexes ranging from subatomic to atomic-level sizes.

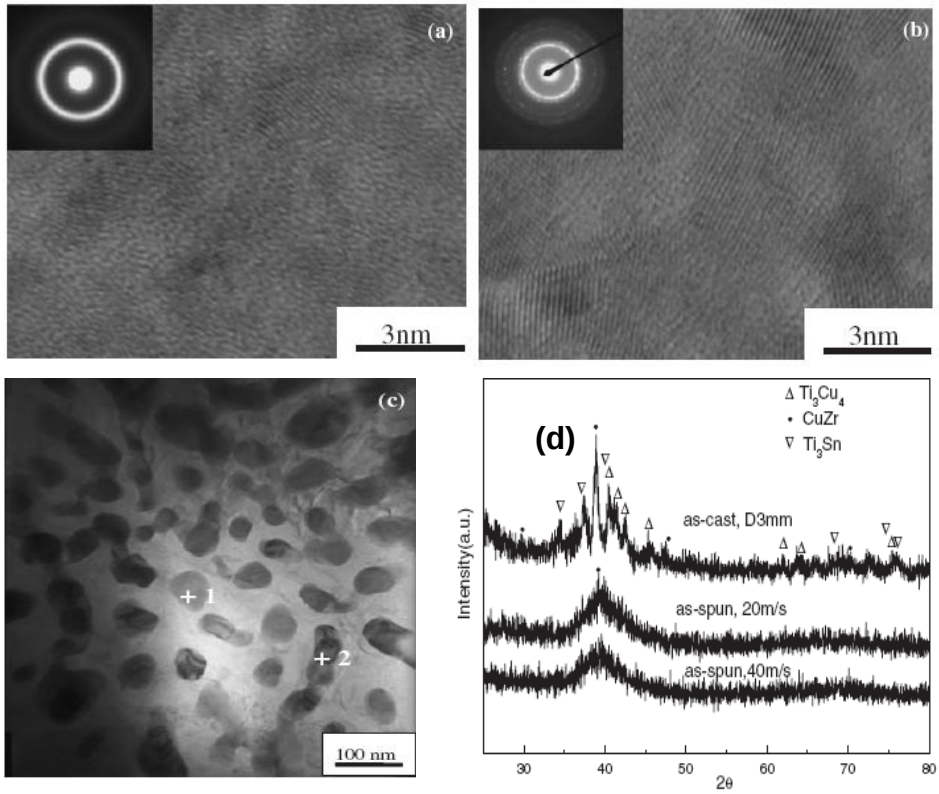

Figure 6. HREM and bright field TEM images and selected area diffraction pattern of the $Ti_{47.5}Zr_{15}Cu_{30}Pd_{7.4}Sn_5$ as spun ribbons and as cast rod; (a) ribbon at 40 m/s, (b) ribbon at 20 m/s, (c) rod (d) XRD pattern of $Ti_{47.5}Zr_{15}Cu_{30}Pd_{7.4}Sn_5$ as spun ribbons and as cast rods [69] (with permission from The Japan Institute of Metals).

The processing parameters have an influence on the structure obtained. This can be seen from the Figure 6(a-c) which shows HREM, bright field TEM images, selected area electron diffraction (SAED) patterns and X-ray diffraction (XRD) of $Ti_{47.5}Zr_{15}Cu_{30}Pd_{7.4}Sn_5$ alloys. Figure 6(a) shows the as-spun ribbon prepared at the speed of 40 m/s where a diffuse halo is observed indicating the main structure is a glassy state. It can be observed in HREM image that some fine nanoparticles are dispersed in the glassy matrix, and in XRD pattern it is seen that no crystalline peaks appear. The SAED pattern of as spun ribbon prepared at 20 m/s (Figure 6(b)) comprise of several rings superimposed on diffuse halo pattern, thus showing the presence of a mixture of nanocrystalline and glassy phase. It was observed that the size and volume fraction of nanoparticles increases with decrease in melt spinning speed. Figure 6(c) shows bright field image and SAED patterns of as-cast $Ti_{47.5}Zr_{15}Cu_{30}Pd_{7.4}Sn_5$ rods. It was clear from the micro-structure of the metallic glass that volume

fraction of nanoparticles increases with decreased cooling rate [69]. Figure 6(d) shows the X-ray diffraction pattern of as-spun ribbons and as-cast rods of $Ti_{47.5}Zr_{15}Cu_{30}Pd_{7.4}Sn_5$.

6. Model Systems for Predicting Structure

Stereo chemically defined model (SCD) was a structural model introduced to describe the atomic arrangement of atoms in metallic glasses (metal-metalloid glasses). This model included atoms of unequal sizes, explained the concept of short range forces and used efficiently packed solute centered clusters of co-ordination number 9 as structural building blocks. From the SCD model a new structural model was derived, called the efficient cluster packing model (ECP).

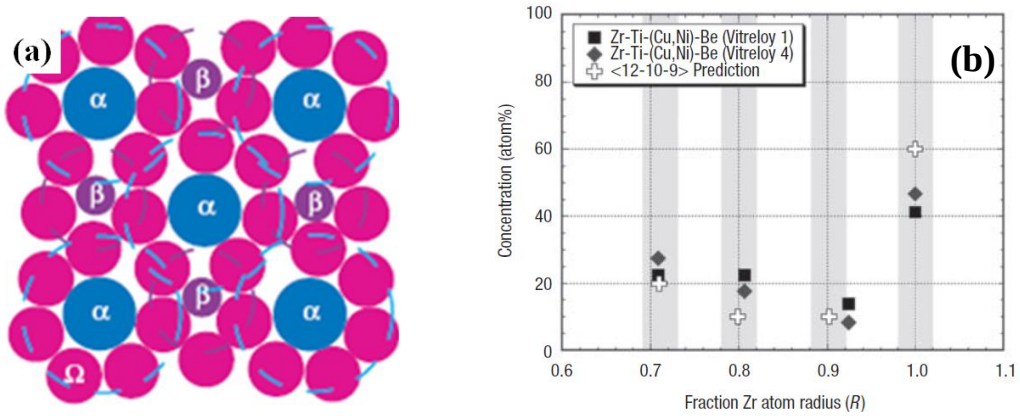

Figure 7. (a) A two dimensional representation of a dense cluster-packing structure in a (100) plane of clusters illustrating the features of interpenetrating clusters and efficient atomic packing around each solute. (b) Comparison of relative atomic sizes and concentration for Zr-based metallic glass with predictions from dense cluster packing model, the <12-10-9> model [72] (with permission from Nature publishing group).

The ECP model could explain the short range and medium range order and density in metallic glasses. Efficient packing is obtained for specific radius ratios between solute and solvent atoms that give solute-lean clusters with a central solute atom surrounded by solvent atoms. The most stable glasses are solute rich [70]. Whereas in Sopu et al. reported a nanoglasses of Cu-Zr binary alloy with Cu-centered full icosahedral short range order topology known to be the key structural motif in amorphous Cu-Zr alloy characterized by high packing density [71]. Another model system called the dense cluster packing model predicts the structure of metallic glasses with more precision. A dense cluster packing model designated as <12-10-9>, where 12, 10 and 9 represent the co-ordination number of α, β, γ which are different atomic species forming the bulk metallic glass based on Zr that contain Be is shown in Figure 7(a) [72]. The structural predictions of <12-10-9> model for Zr-Ti-(Cu, Ni)-Be BMG seem to be in well agreement with its established structure (Fig 7b). Efficiently packed structures are expected to have reduced kinetics and fragility, but quantitative connection between structure and kinetics is yet to be resolved.

7. Metallic Glass Properties

7.1. Electrical properties

Electrical conductivity of metallic glasses is generally two orders of magnitude lower than that of their crystalline counterparts. The very low conductivity of metallic glasses is due to their intrinsic disordered structure. By forming composites of bulk metallic glasses its conductivity can be improved. Wang et al. reported $Ni_{59}Zr_{20}Ti_{16}Si_2Sn_3$ bulk metallic glass composite containing 40 vol% α brass was shown to have improved electrical conductivity than monolithic BMG [73]. Figure 8 (a and b) shows temperature dependence of electrical resistivity in monolithic and composite BMG, respectively.

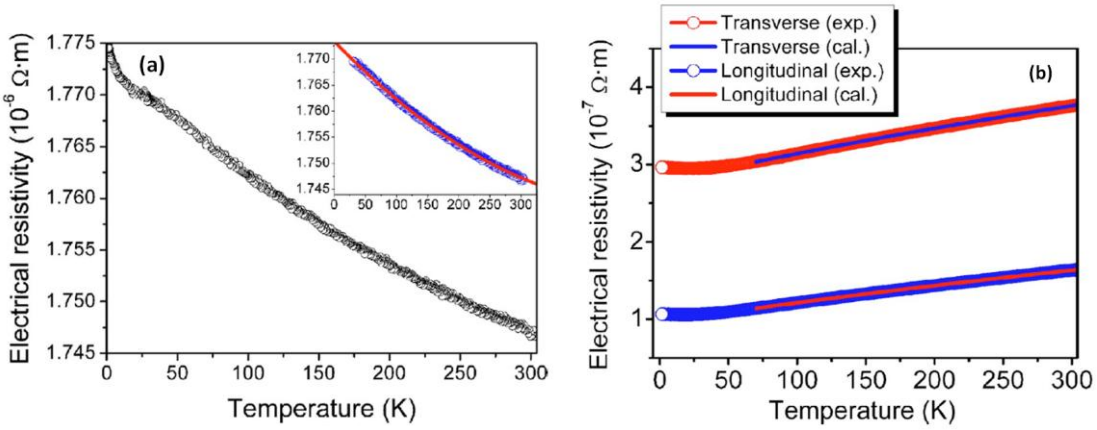

Figure 8. Temperature dependence of electrical resistivity (a) monolithic Ni-based BMG and (b) BMG composite in the longitudinal and transverse directions at temperature ranging from 2 to 300 K [73] (with permission from American Institute of Physics).

In composite BMG, the resistivity along the longitudinal direction is three times smaller than that along transverse direction. This difference indicates that the conductivity of composite is anisotropic and sensitive to morphology of high conducting phase [73,74]. The conductivity of binary composites with a randomly distributed high-conductive phase has been found to follow percolation theory. Umetsu et al. [74] showed the behavior of the temperature dependence of the electrical resistivity of Zr-based amorphous alloys is discussed in connection with the value of the temperature co-efficient of resistivity (TCR). The values of TCR for x = 0, 5, 10 in $Zr_{55}Al_{10}Cu_{35-x}Ni_x$ are −13.6, −15.7 and −20.5 × 10^{-5} K^{-1}, respectively. It is considered that the absolute value becomes larger with increasing Ni content. The electrical resistivity at room temperature of $Zr_{42}Cu_{42}Ag_8Al_8$ BMG alloy is about 170 × 10^{-8} Ω m and the value of TCR is 3.2 × 10^{-5} K^{-1}. The temperature dependence of electrical resistivity of as cast BMG and after heating is shown in Figure 9.

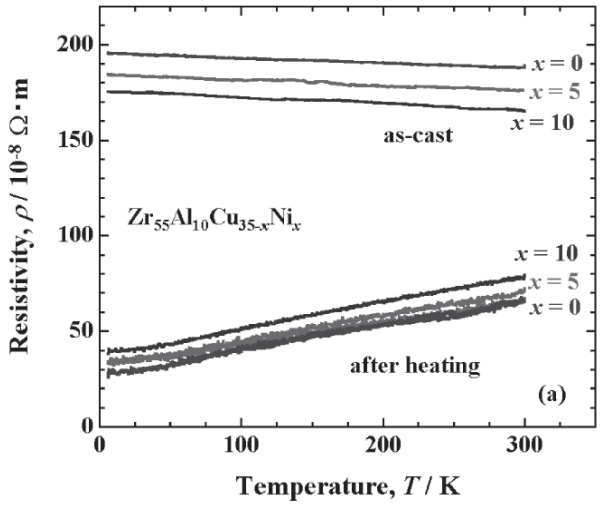

Figure 9. Temperature dependence of the electrical resistivity of $Zr_{55}Al_{10}Cu_{35-x}Ni_x$ (x= 0, 5 and 10) bulk metallic glassy alloys, as cast and after heating upto 873 K [74] (with permission from The Japan Institute of Metals).

In case of TFMG, the temperature dependence of resistivity is different from the BMG leading to dramatic increase in the electrical resistivity in supercooled liquid region. This is due to the fact that the random atomic structure in the amorphous phase is believed to cause the electrical resistivity increase within supercooled liquid region (ΔT), while the presence of crystalline phases in the films annealed at temperatures other than ΔT result in relatively low resistivity [21]. In case of $Cu_{51}Zr_{42}Al_4Ti_3$ TFMG, increase in the electrical resistivity to a maximum of ~4628 μΩ cm at 502 ℃ was observed and the resistivity decreases to ~177 μΩ cm while the temperature reaches 527 ℃ [21].

7.2. Mechanical Properties

The mechanical properties of BMGs can be described in terms of Yield Strength, Fracture Strength and Vickers Hardness. The yield strength and fracture strength have a linear correlation with Vickers hardness and Young's modulus [75]. Bulk metallic glasses are isotropic solids. Hence the mechanical properties are much less dependent on the processing history in case of metallic glasses. Whereas for crystalline alloys the microstructure can be modified according to the process involved, resulting in different mechanical properties. Structural relaxation on annealing does not affect the yield strength or hardness values. BMGs tend to break after yielding at ambient temperature. At low temperatures the inhomogeneous plastic flow of BMGs occurs by propagation of shear bands which are 10–20 nm thick and make steps on the surface up to several micrometers in height. A strongly localized shear deformation at room temperature [77] limits practical application of such materials since a shear event may trigger a crack nucleation and rapid fracture. It is seen that fracture of bulk metallic glasses is very responsive to macroscopic defects like pores and surface imperfections which explains large scattering in the values of the percentage deformation changing from sample to sample [78]. Different specimen geometries control the shear band formation and deformation processes, resulting in variations of mechanical properties. Localised shear deformation may trigger a crack nucleation and rapid fracture.

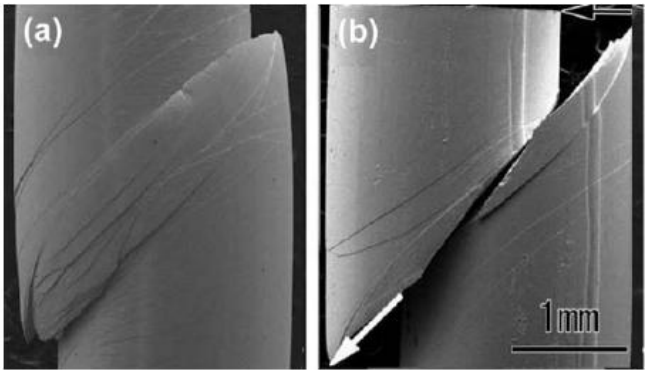

Figure 10. Two regimes of deformation observed in metallic glasses: (a) relatively homogeneous deformation with many shear bands in the $Zr_{62.5}Cu_{22.5}Fe_5Al_{10}$ BMG and stick-slip behavior in a single major shear band in the $Zr_{67.5}Cu_{17.5}Fe_5Al_{10}$ BMG (Scanning Electron Microscope) [76] (with permission from Elsevier).

As a localized shear deformation is a main plastic-deformation mode at room temperature tensile ductility is not seen in bulk metallic glassy samples except in a few special cases at high strain rates [79]. Some BMGs ($Zr_{62.5}Cu_{22.5}Fe_5Al_{10}$) demonstrate the formation of multiple shear bands (Figure 10(a)), while others ($Zr_{67.5}Cu_{17.5}Fe_5Al_{10}$) deform through a major single shear band leading to crack formation (Figure 10(b)).

For improving the ductility of metallic glasses, the formation of heterogeneous microstructures in a composite manner is essential and employed in a variety of procedures combining a glassy matrix with second phase crystalline particles [80]; the deformation-induced nanocrystallization [81] is one of the possible ways illustrating this approach. One of the ways is to obstruct the propagation of shear bands through the sample by interaction with the phases embedded into glassy matrix. This enables multiplication, branching and termination of the shear bands similar to the composites where cracks are either blocked by reinforcements or blunted in ductile phases or matrix. The blockage of the crack-tip area by nanoparticles stabilizing plastic deformation was observed in $Cu_{50}Zr_{50}$ as well as in the $Zr_{65}Al_{7.5}Ni_{10}Pd_{17.5}$ glassy alloys [82]. The compressive room-temperature stress-strain curves of the $Zr_{65}Al_{7.5}Ni_{10}Cu_{17.5}$ and $Zr_{65}Al_{7.5}Ni_{10}Pd_{17.5}$ bulk metallic glassy alloys revealed significantly different plasticity of these alloys ,though both of the alloys possess a glassy structure, because by substitution of Cu by Pd, the primary phase changes into nanoscale icosahedral quasicrystalline phase. These nanoscale structures contribute to mechanical properties like good strength and ductility [83].

Considering mechanical properties of thin film metallic glasses, Coddet et al. [84] reported that in amorphous Zr-Cu-(N) films obtained for Cu contents between 25 and 75 at% both hardness and Young's modulus increase with Cu content. This can be attributed to the decrease of the average interatomic distance as well as to a higher strength of atomic bonds. Increase in the Cu content results in denser atomic packing state which encourages higher hardness and higher Young's modulus. In case of $W_{46}Ru_{37}B_{17}$ and $W_{45}Re_{23}Ru_{15}B_{17}$ TFMGs, the hardness has high values over 15 GPa upto 700 K and over 10 GPa upto 900 K, but then decreases rapidly at high temperature towards a very small minimum at around the glass transition temperature, where amorphization takes place [85]. Ye et al. measured hardness and elastic modulus using a sequential nanoindentation technique [39]. This technique consists of numerous loading, holding and unloading cycles and using

the Oliver-Pharr approach, the elastic modulus of the film was obtained after each load cycle. A comparison of hardness versus modulus relation of BMGs and TFMGs obtained from indentation testing [86−89] revealed that this elastic modulus increases with indentation depth due to substrate effect. The hardness of TFMGs remains constant for the indentation depth falling below 10% of the corresponding film thickness, which was selected to be materials intrinsic property.

Ye demonstrated that with focused ion beam micromachining composite (TFMG/Si) micropillars can be fabricated of different size and shapes [39]. By micromachining, the influence of Si substrate on the yielding and post yielding behavior can be tuned by deliberately adjusting the ratio of film thickness to pillar diameter. From microcompression, the elastic moduli and yield strength of TFMG layer on the substrate can be measured. The typical load-displacement curves obtained from the micropillars of different sizes and shapes. A composite elastic modulus of the micro-pillar could be derived after taking into consideration the tapering of the focused ion beamed micropillar and the substrate conformity. Thus, the elastic modulus of the TFMG top layer can be obtained by subtracting the stiffness of the Si substrate out of total stiffness of the micropillar. Since, Si substrate is much stronger than the TFMG layer, the yield strengths, σ_y, of the TFMGs can be derived from load-displacement curves of the composite micropillars. As load-displacement curves varies with micropillars of different shapes, the yield strength obtained from it also varies with the focused ion beam-milled micropillars (figure 11).

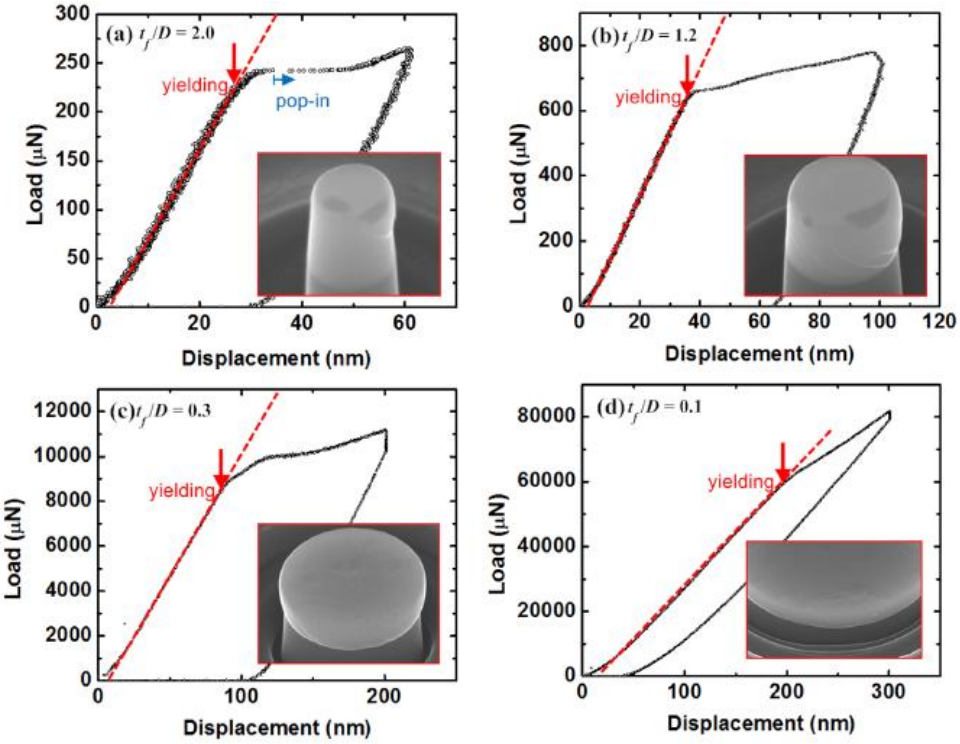

Figure 11. The typical load-displacement curves obtained from the microcompression of TFMG/Si composite micropillars with the same film thickness of 600 nm but different film thickness to diameter ratios. Insets show the SEM micrographs of the corresponding micropillars after microcompression [39] (with permission from American Institute of Physics).

The yield strength obtained as a function of t_f/D (film thickness to pillar diameter ratio) ratio revealed the yield strengths of TFMGs can be viewed as a constant at 2.6 GPa for $t_f/D > 0.5$; however when $t_f/D < 0.5$, a substrate effect arises leading to the increasing yield strength with the decreasing t_f/D ratio [90].

7.3. Tribological Properties

Excellent mechanical properties are a sign of promising tribological properties. Blau [91] showed no amorphous to crystalline (or vice versa) transformation evidence on worn surface in case of ZrCuNiTiAl metallic glasses while in Fu and coworkers [92] reported that in the Zr-based BMGs not only crystallization occurred on amorphous metallic glasses during tribological contact but also crystalline metallic glasses are re-amorphized. Zeynep and coworker have compared the coefficient of friction of $Zr_{52.5}Ti_5Cu_{17.9}Ni_{14.6}Al_{10}$ with aluminum 6061 and Stainless Steel AISI 304. Here block on ring set up was used to study friction and wear properties [93]. Zr-based BMG has lower co-efficient of friction than that of aluminum and stainless steel. During sliding, the wear rate decrease is controlled through the material transfer phenomenon between the counter surface material on the block on ring set up and the formation of protective oxide layers on the Zr-based BMG surface. The co-efficient of friction first rises due to initial damage on major surface asperities at lower loads and then decreases due to compacted and flattened debris at higher loads. The hardest material, Zr-based BMG has the highest wear rate, contrary to what is expected [94]. High wear rate of the Zr-based BMG is explained by their poor ductility in tension [95], because the BMG experiences a high tensile stress during abrasive wear processes. The lowest hardness material being Aluminum, (out of Zr-based BMG, Aluminum and Stainless Steel) has better wear rate than that of stainless steel due to the rule of identical metal couple [96].

In another study conducted by Jang et al. [97], under the normal load of 1.4 kgf and sliding speed of 0.1 m/s the coefficient of friction and wear rate of three BMGs were cross-checked i.e. $Fe_{73.97}C_{9.60}Si_{1.82}P_{5.81}Cr_{2.57}Al_{0.81}Mo_{5.23}$, BMG1 + 50% Ni-base self flux alloy and BMG1 + 25% Ni-base self flux + 25% WC. The friction coefficient value for $Fe_{73.97}C_{9.60}Si_{1.82}P_{5.81}Cr_{2.57}Al_{0.81}Mo_{5.23}$ was stabilized in the range of 0.35~0.4 after around 1200 sec. For , BMG1 + 50% Ni-base self flux alloy and BMG1 + 25% Ni-base self flux + 25% WC, much lower values ranging from approximately 0.08 to 0.15 were obtained upto 2,500 sec, while for the crystalline materials, AISI 304 and AISI52100, the average friction coefficient values were in the range of 0.35~0.5 regardless of the material's hardness values. The wear rates of the BMG samples were found to be much lower than those of AISI304 under the test conditions. Whereas the wear rate of AISI52100 depended on its hardness value. AISI 52100 showing a hardness value of Hv300 has a higher wear rate than BMGs , and for one with a hardness of HV840 the wear rate was lower than BMG1 + 25% Ni-base self flux + 25% WC.

The adhesion properties of TFMGs show wide variations with composition, deposition technique, and substrate. In case of $Zr_{47}Cu_{31}Al_{13}Ni_9$ metallic glass films on 316L, stainless steel, a high density of shear bands is formed along the sliding direction with ductile deformation mode with good film plasticity [98]. In recent work, $Zr_{58}Cu_{25}Al_{11}Ni_6$ deposited on Si (001) by pulsed DC magnetron sputtering [21], the mean COF value was around 0.3–0.4 and no apparent crack or delamination was found adjacent to the scratch track of the coating, suggesting good adhesion.

7.4. Corrosion Behavior

Chunling et al. carried out, corrosion studies on $(Cu_{0.6}Zr_{0.3}Ti_{0.1})_{100-x}Nb_x$ (x = 0–5 at%)**.** Potentiodynamic polarization curves were measured with a potential sweep rate of 50 mV min^{-1} [99]. The corrosion rates were estimated from the weight loss after immersion. Electrochemical measurements were conducted in a three electrode system using platinum as counter electrode and Ag/AgCl reference electrode. The corrosion behavior of the $(Cu_{0.6}Zr_{0.3}Ti_{0.1})_{100-x}Nb_x$ (x = 0–5 at%) samples were tested in 1N HCl, 3% NaCl, 1N HNO_3, 1N NaOH solutions. As the Nb content increases corrosion rate decreases in all solutions. Cu-Zr-Ti-Nb alloys show high corrosion resistance to alkaline solution like NaOH as they show no weight loss after immersion in NaOH solution for 336 hr. Whereas when immersed in 1N HCl and 3% NaCl solutions, with increase in Nb content the corrosion rate of $(Cu_{0.6}Zr_{0.3}Ti_{0.1})_{100-x}Nb_x$ (x = 0–5 at%) was seen to decrease. Figure 12 (a-d) shows polarization curves in 1N HCl, 3% NaCl solutions, 1N H_2SO_4, and 1N HNO_3 solutions. The glassy alloy's shows increase in anodic current densities when there is a slight anodic polarization. With increase in Nb content the glassy alloys show nobler corrosion potential and lower anodic current densities, thus showing higher corrosion resistance. Cu is an unstable element in electrolytes open to air, hence the corrosion rate of the metallic glass increases if the concentration of Cu is high on the surface. It was elucidated that the Nb depresses the diffusion of Cu to the surface thereby improving the corrosion resistance.

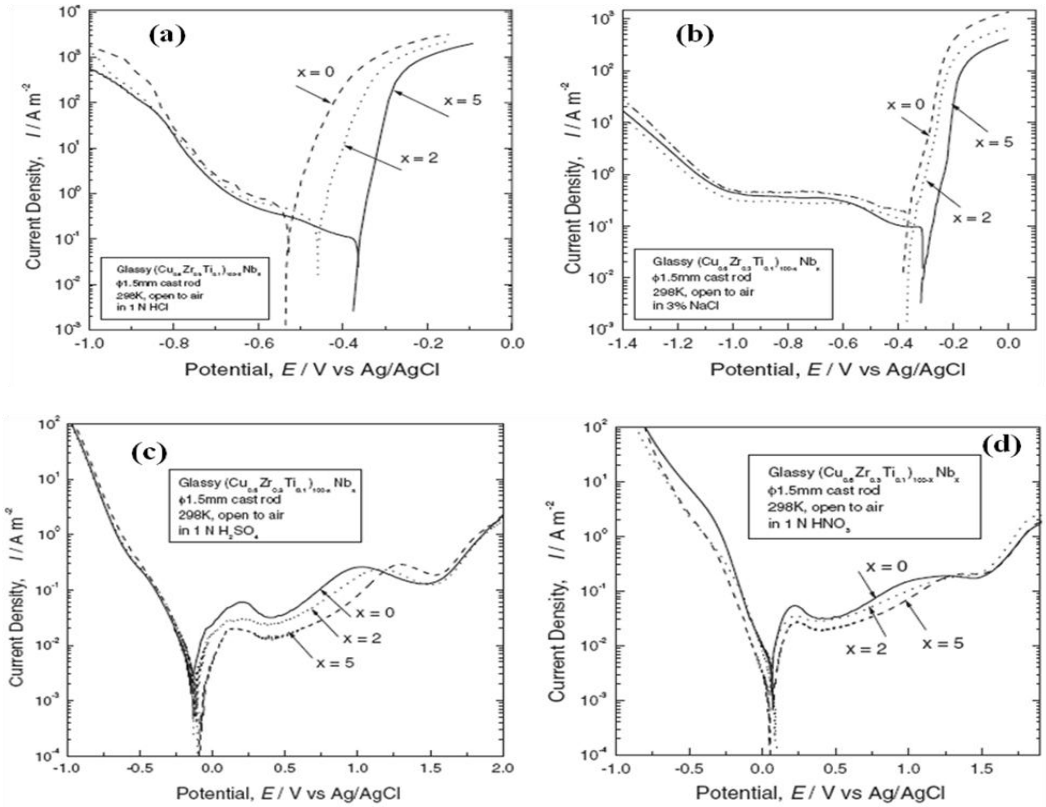

Figure 12. Potentiodynamic polarization curves of the $(Cu_{0.6}Zr_{0.3}Ti_{0.1})_{100-x}Nb_x$ bulk glassy alloys in (a) 1N HCl, (b) 3% NaCl,(c) 1N H_2SO_4 and (d) 1N HNO_3 [99] (with permission from The Japan Institute of Metals) .

Qin and coworkers performed corrosion studies of $Ti_{40}Zr_{10}Cu_{36}Pd_{14}$ BMGs in Hank's solution by performing electrochemical measurements in the same on samples annealed at 693 K, 723 K and 823 K [100]. Potentiodynamic polarization curves were measured with a potential sweep rate of 0.83 mV in Hank's solution. It was observed that passive current densities and pitting potentials in Hank's solution are dependent on the annealing temperature. The as cast bulk metallic glass and its crystalline alloys have lower passive current densities than commercially available Ti-6Al-4V, indicating better corrosion resistance by denser passive film formation.

In a work by Vincent et al. corrosion study was performed on $Cu_{60}Zr_{20}Ti_{20}$ (at%) metallic glass in acidic and neutral Cl^- solution [101]. Samples were evaluated by electrochemical polarization experiments. On performing potentiodynamic polarization measurements it was found that the higher the concentration of chloride ions the higher is the icorr value i.e. the rate of corrosion increases with increase of Chloride ions in NaCl solution. 304L Stainless steel has E_{corr} value of −0.69V (vs Standard Calomel Electrode) in 1M NaCl , while that of $Cu_{60}Zr_{20}Ti_{20}$ metallic glass is −0.30V (vs SCE). This shows that $Cu_{60}Zr_{20}Ti_{20}$ is nobler than 304L stainless steel.

Thin film metallic glasses also show corrosion resistance if coated evenly on a substrate. In the work reported by Li-Ting Chen et al. [102], corrosion study was performed on Fe-Zr-Ti TFMG coated AISI420 discs and on bare AISI420 by performing potentiodynamic polarization in NaCl aqueous solution. For the coating with lower Fe content the corrosion resistance of the Fe-Zr-Ti TFMG coated AISI420 discs is very similar to the bare AISI420 substrate, whereas for the TFMGs with higher Fe content, the lower current density and higher polarization resistance than those of AISI420 substrate are observed. The corrosion density increases to 10^{-4} A/cm^2 due to spontaneous passivation behavior and large passive regions.

7.5. Magnetic Properties

Inoue and co-workers produced multi-component Fe-based bulk magnetic systems displaying soft magnetic properties containing a very large number of elements [103]. Since then a variety of Fe-based, Co-based and Ni-based bulk glassy alloys have been produced on the basis of the three component empirical rules [15]. They developed BMG rods (1–12 mm diameter) of composition $RE_{60}Fe_{30}Al_{10}$ (RE = Nd or Pr) with appreciable coercivities at room temperature that can make this composition to] be considered as hard [104]. Co-based metallic glasses with a coercivity below 1 A/m also show a very low saturation magnetostriction constant of the order of ks = 10^{-7} ppm [105].

Pookat et al. studied the magnetic properties of sputtered CoFe based TFMG obtained from $Co_{75}Fe_{14}Ni_4Si_5B_2$ target [48]. Low remanence was observed in the as-deposited film, indicating demagnetization along the in plane direction due to island shaped structures present in the sample. Atomic force microscopy revealed the island shaped structures of 500 nm size [48]. The relatively high value magnetostriction observed for CoFe thin films increases the levels of stress developed during the growth of CoFe films. The magnetic properties depend on film thickness, composition, surface/interface roughness. Enhanced magnetic softness compared to their polycrystalline counterparts can be achieved by thermal annealing near crystallization temperature or by electron ion beam irradiation. Annealing of amorphous alloy thin films causes the relaxation of amorphous structure and initiates the formation of a composite amorphous/crystalline microstructure. This microstructure helps improve the soft magnetic properties.

Chu et al. studied the magnetic properties of as deposited and annealed sputtered $Fe_{65}Ti_{13}Co_8Ni_7B_6Nb_1$ film [106]. The films exhibited soft magnetic behavior below the exothermic peak (from differentially scanning calorimetry scan) at 911 K and the lowest coercivity and saturated magnetization at 898 K (Figure 13). Strong perpendicular magnetic anisotropy with magnetic easy axis normal to the plane of the film occurred at 923–973 K, thus forming strongly contrasting dark and bright stripes magnetic domain in MFM images. As the magnetization is along the easy axis and normal to the film plane, the demagnetizing fields in the film increase. It was observed that to minimize this demagnetizing fields, dark and bright stripe domain structures were formed. As the MFM tip is magnetized downwards, the bright stripes are domains with magnetization upwards and dark stripes are regions with magnetization downward. This normal or perpendicular magnetic anisotropy can be attributed to internal stress caused by lattice strain. The presence of FeNi nanocrystals with larger lattice structure in the small Fe (Ni) matrix above 923 K generated compressive stress [106].

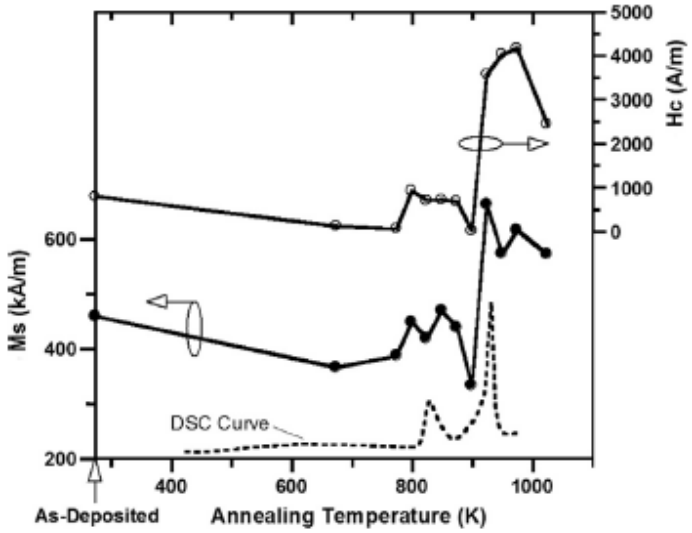

Figure 13. Variation of film coercivity (Hc) and saturation Magnetisation (Ms) with annealing temperature along with DSC thermogram included for comparison [106].

8. Applications

8.1. Optoelectronics Application

A number of studies have been initiated to unravel the optical transmittance and reflectivity of TFMGs when applied to substrates like polyethylene terephthalate (PET) and glass. The smooth surface, negative heat of mixing, absence of grain boundaries of TFMGs make them ideal for applications aimed at improving the optical transmittance or reflectivity of devices used to harvest solar energy [107]. Indium tin oxide being a transparent conductive material used in various applications [108]. A bilayer structure of ITO/ZrCu (IZC) is used to produce transparent conductive electrodes on a PET substrate to avoid high cost of indium without obstructing the optical transmittance of ITO. For comparison Ag layer was introduced to form ITO/Ag (IA) films. In order

to create a ITO-metal-ITO layer with a continuous metal layer of TFMG between the sandwich layers was used for the continuity of the metallic layer. Transmittance was shown to decrease with an increase in thickness of the ZrCu films. The reflectivity of IA films at wavelengths exceeding 550 nm depicted an increase with increase in thickness of Ag layer. The apparent difference between Ag and ZrCu TFMGs were attributed to the microstructures they form when produced in very thin layers. ZrCu layers were smooth whereas the Ag layers had discontinuous island structures. The negative heat of mixing in TFMGs led some researchers to assume that these materials might provide means to produce thin (less than 6 nm) continuous metal layer for ITO-metal-ITO transparent conductive electrodes. In a study by Hu et al. [109], they suggested that in all multicomponent alloys, the reflectivity is a function of electrical resistivity and amorphous alloys show higher scaling coefficient than crystalline counterparts. This is mainly because of a longer mean free time for charge carriers in the amorphous alloys.

8.2. Biomedical application

The growth of C. albicans, E. coli and P. aeruginosa, were studied for incubation time of 24, 48, and 72 h on TFMGs reveal better antimicrobial activity than stainless steel. ZrCuAlAg1, ZrCuAlAg2 and ZrCuAlAg3 show complete inhibition in 72 hrs [110]. These coatings can be given on stainless steel door handles, surgery equipments in a hospital environment where hands come in contact. C. albicans has resistance to Cu [111]. The high copper tolerance is one of the reasons that ZrAlNiCuSi TFMGs only have an antimicrobial activity of C. albicans within incubation times of 24 hrs. Biofilm formation of C. albicans is disrupted by small size and well dispersed silver nanoparticles. ZrCuAlAg TFMGs reveal superior antimicrobial activity against C. Albicans, as silver particles are dispersed in the matrix. E. coli growth is hindered better by as-deposited ZrCuAlAg TFMGs than stainless steel. The growth of E. coli has been restricted on ZrCuAlAg1 and ZrCuAlAg2 coatings due to the presence of Cu and Ag, and fine surface morphology. All TFMGs show good antimicrobial activity for entire period of incubation. Method by which Cu and Ag ions lose its effectiveness is a matter under study.

Chu et al. studied the antibacterial properties of $Zr_{53}Cu_{33}Al_9Ta_5$ and $Cu_{48}Zr_{42}Ti_4Al_6$. Both TFMGs were shown to prevent growth of E. coli by attaining an antibacterial rate value of 100% [112]. Whereas for S. aureus the Cu based TFMG was less effective probably due to difference in peptidoglycan thickness when compared to E. coli. Chu et al. [113] studied the antimicrobial performance against Staphylococcus aureus, Escherichia coli and Pseudomonas aeroginosa on $Al_{48}Ag_{37}Ti_{15}$, $Zr_{54}Ti_{35}Si_{11}$ and $Zr_{59}Ti_{22}Ag_{19}$ TFMGs. It was observed that $Zr_{54}Ti_{35}Si_{11}$, with no Ag or Al showed poor antimicrobial capability.

Metallic glasses have emerged as new class of biomaterials. Their prominent properties include high strength, elasticity, corrosion resistance [114]. Metallic glasses thin films are a new material for biomedical devices formed by thermoforming. There are several reports of thermoform microdevices using polymers [115]. These polymers can be replaced by metallic glasses for improved properties. Biomimetic micro or nanoscale surface can be obtained by imprinting metallic glasses for microdevices.

Schroers et al. [4] showed that metallic glasses have corrosion resistant property hence can be used in physiological conditions. In vitro studies show that $Zr_{44}Ti_{11}Cu_{10}Ni_{10}Be_{25}$ and $Pt_{57.5}Cu_{14.7}Ni_{5.3}P_{22.5}$ metallic glasses have better cell adhesion and proliferation of mouse fibroblasts

in when compared to commercially available biomaterials. Metallic glasses showed better bioactivity than crystalline phase materials. Their improved bioactivity, polymer-like formability, corrosion resistance, and excellent mechanical properties makes them a suitable biomaterial.

Kaushik et al. [116] reported TiCuNi films with good biocompatibility on muscle cells. The films of TiCuNi sputter deposited on Si substrate and having an amorphous structure has high mechanical and wear resistant properties. In-vitro studies for biocompatibility analysis proved that the TiCuNi films to be non toxic to mammalian cells and are suitable for cell growth, proliferation and tissue formation. Imprintability like polymers was seen in this TFMG which established that they could assure required precision and repeatability to shape complicated geometries used in biomedical applications. They can be coated on any non biocompatible material for biomedical applications.

8.3. Micro Electromechanical System (MEMS)

Market for microspeakers is growing per year. MEMS loud speakers are produced using metallic glass membranes SiN layer on top of SiO_2/Si wafer. Later Si cavity wet etching was performed. On this Pd-based alloy was deposited by sputter coating. Then SiN layer was also etched out (dry etching). Leaving metallic glass coating exposed. A magnetic paste consisting of NdFeB particles was deposited (screen printed) on metallic glass membrane. This was subjected to curing and then magnetization to form integrated permanent magnet. Metallic glass is promising wherever large elastic deformations are needed. Today the Poly-Si membrane in MEMS microphones is increasingly replaced with metallic glass [117].

Pd-, Zr, and Cu based thin film metallic glass fabrication enable fabrication of very planar structures by easing the internal stress critical in MEMS fabrication and three dimensional structures can be created through microforming using the supercooled liquid region [118]. Recently, Junpei et al. reported that Ni-Ti-Zr TFMGs as shape memory alloys can be used in MEMS with three dimensional structures [119].

8.4. Thin Film Metallic Glass as Hydrogen Sensors

Hydrogen sensors are required in fuel cell vehicles and other environmental monitoring processes. Due to high corrosion resistance and excellent mechanical properties Pd-Cu-Si metallic glasses were found to be promising material for hydrogen sensing applications [120]. The H_2 response was measured by changes in electrical resistance of films exposed to N_2 and H_2. Pd was the element responsible for hydrogen absorption in the Pd-Cu-Si alloy, therefore H_2 response increases with Pd content. The response time of hydrogen sensors made with thin film metallic glasses was quite fast.

8.5. Bulk metallic glass as Machinery parts

High torque geared motors were produced with outer diameter of 1.5 and 2.4 composed of sun-carrier, planet-type gears, gear axis and bearing made of Zr, Cu, Ni and Fe-based glassy alloys [121]. The endurance limit when compared time is much longer than that of conventional tool steel and difference is 32 times for Zr-based alloys. The rotation of motor using SK4 gears stopped 8 hrs, whereas Ni-based glassy alloy gear had the original shape even after 2500 hrs. Wear resistance is

highest for Fe-based glassy alloy > Ni-based glassy alloy > Cu-based glassy alloy > Zr-based glassy alloy > conventional tool steel (SK4). The wear loss of Fe-based glassy alloy is one-third smaller than Ni-based glassy alloy signifying that the wear resistance of their bulk glassy alloys is much better than that of SK4 steel. The cause for improved wear resistance is supposedly due to the effect of smooth outer surface without grain boundaries, homogenous structure without appreciable component segregation and high corrosion resistance, high hardness, low Young's modulus, large elastic elongation, high toughness and high fatigue strength.

8.6. Miscellaneous

BMGs find various application in commercial market for example, as striking face plate in golf clubs, frame in tennis racket, various shapes of optical mirrors, casing in cellular phones, casing in electro-magnetic instruments, connecting part for optical fibers, soft magnetic high frequency coils, shot penning balls, high torque geared motor parts, electromagnetic shielding plates, soft magnetic choke coils, high corrosion resistance coating plates, vessels for lead free soldering. Other applications include, higher sensitivity type, higher load type and smaller size pressure sensors in automobiles, Colliori type liquid flow meter, spring, slat truck cover for air plane, in-printing plate, high density information storage material, high frequency type antenna material, yoke material for linear actuator, magnetic iron core for high rotation speed motor, biomedical instruments such as endoscope parts [122]. Due to BMG's toughness it is used as aircraft part and also used as fuel-cell separator due to anti-corrosion properties.

9. Future Prospects

Considering the significant rapid progress in bulk metallic glass forming alloys made for the last one decade, it is expected that subsequent study leads to the production of bulk glassy alloys with diameter of 30 to 50 mm. When future prospects of engineering Fe-, Co-, Ni-, and Cu-based metallic glass alloys are extensive, the key point is accredited to the possibility of extending the processes for larger scale production with diameter of greater than 30 mm. The right composition for obtaining the desired amorphous phase is still an open challenge. Despite substantial progress in modeling and simulation of glass forming ability, identifying the eutectic phases through phase diagram is followed at large which is still a trial and error approach. Therefore, while exploring new TFMGs it is critical to achieve the right combination of elements which would lead to amorphous state and the process is considered as a surmount bottleneck for MEMS/Bio-MEMS device fabrication.

10. Conclusion

This paper in general tries to throw light on processes involved in production of bulk metallic glasses which are suction casting, melt spinning, splat quenching, mould casting and centrifugal mould casting and also surface treatment processes like laser ablation, plasma immersed ion implantation and electrodeposition. Thin film metallic glasses are formed by micro-technological processes like sputter deposition, pulsed laser deposition, thermal evaporation and electron beam evaporation. Structural models for predicting atomic arrangement in metallic glasses was briefed. In glass transition kinetics the concept of fragility for glass forming liquids was introduced through

parameter, fragility index. Fragility index indicates if the system is a strong glass former or fragile. The electrical, mechanical and tribological properties of BMGs were discussed. Corrosion behavior of BMGs and TFMGs in different metallic glass compositions in different media was reviewed. It was seen that metallic glasses have good corrosion resistant, which opens up possibility for development of MEMS and Bio-MEMS devices. This review tries to bring into light the process-structure-property relation understanding crucial for designing and developing unique materials for different applications. The paper concludes by discussing various applications of TFMGs and BMG. Future prospects of metallic glasses lies in better understanding of formation of metallic glasses.

Acknowledgement

The authors thank PSG Institute of Advanced Studies, Coimbatore for providing platform for undertaking this review study.

Conflict of Interest

The authors declare that there is no conflict of interest regarding the publication of this manuscript.

References

1. Klement WJ, Willens RH, Dumez P (1960) Non-crystalline Structure in Solidified Gold-Silicon alloys. *Nature* 187: 869–870.
2. Tsai PH, Li JB, Chang YZ (2014) Fatigue properties improvement of high-strength aluminum alloy by using a ZrCu-based metallic glass thin film coating. *Thin Solid Films* 561: 28–32.
3. Chu JP, Huang JC, Jang JSC (2010) Thin film metallic glasses: Preparations, Properties and Applications. *J Miner Met Mater Soc* 62: 419–424.
4. Schroers J, Kumar G, Thomas M (2009) Bulk metallic glasses for biomedical applications. *Bio Mater Dev* 61: 21–29.
5. Subir S (1992) Icosahedral ordering in supercooled liquids and metallic glasses. *Bond Orientational order in Condensed Matter System*. KJ Strandburg ed., Springer-Verlag, New York, 255–283.
6. Inoue A (2000) Stabilization of metallic supercooled liquid and bulk amorphous alloys. *Acta Mater* 48: 279–306.
7. Inoue A (2001) Bullk amorphous and nanocrystalline alloys with high functional properties. *Mater Sci Eng A* 304: 1–10.
8. Turnbull D (1969) Under what conditions can a glass be formed. *Contemp Phys* 10: 473–488.
9. Chu JP, Lee CM, Huang RT (2011) Zr-based glass-forming film for fatigue-property improvements of 316L stainless steel annealing effects. *Surf Coat Tech* 205: 4030–4034.
10. Sun YT, Cao CR, Huang KQ (2014) Understanding glass-forming ability through sluggish crystallization of atomically thin metallic glassy films. *Appl Phys Lett* 105: 051901-051901-4.
11. Ramakrishna BR (2009) Bulk metallic glasses: Materials of future. *DRDO Sci Spectrum*.
12. Inoue A, Zhang W (2004). Formation, thermal stability and mechanical properties of Cu-Zr and Cu-Hf binary glassy alloy rods. *Mater Trans* 45: 584–587.

13. Kwon OJ, Kim YC, Kim KB (2006) Formation of amorphous phase in the binary Cu-Zr alloy system. *Met Mater Int* 12: 207–212.
14. Samwer K, Johnson WL (1983) Structure of glassy early-transition-metal-late-transition-metal hydrides. *Phys Rev B* 28: 2907–2913.
15. Schwarz RB, Johnson WL (1983) Formation of an amorphous alloy by solid state reaction of the pure polycrystalline metals. *Phys Rev Lett* 51: 415–418.
16. Linker G (1986) Strain induced amorphization of niobium by boron implantation. *Solid State Commun* 57: 773–776.
17. Sziraki L, Kuzmann E, El-SharifM (2000) Electrochemical behavior of electrodeposited strongly disordered Fe-Ni-Cr alloys. *Electrochem Commun* 2: 619–625.
18. Schwarz RB, Petrich RR, Saw CK (1985) The synthesis of amorphous NiTi alloy powders by mechanical alloying. *J Non-Cryst Solids* 76: 281–302.
19. Mingwei Chen (2011) A brief overview of bulk metallic glasses. *NGP Asia Mater* 3: 82–90.
20. Chang YZ, Tsai PH, Li JB (2013) Zr-based metallic glass thin film coating for fatigue-properties improvements of 7075-T6 aluminium alloy. *Thin Solid Films* 544: 331–334.
21. Chu JP, Jang JSC, Huang JC, et al. (2012) Thin film metallic glasses: Unique properties and potential applications. *Thin Solid Films* 520: 5097–5122.
22. Yu P, Chan KC, Xia L (2009) Enhancement of strength and corrosion resistance of copper wires by metallic glass coating. *Mater Trans* 50: 2451–2454.
23. Huang HS, Pei HJ, Chang YC (2013) Tensile behaviors of amorphous ZrCu/nanocrystalline-Cu multilayered thin film on polyimide substrate. *Thin Solid Films* 529: 177–180.
24. Mohan RS, Jurgen E, Loser W (2002) Cooling rate evaluation for bulk amorphous alloys from eutectic microstructures in casting processes. *Mater Trans* 43: 1670–1675.
25. Stoica M, Bardos A, Roth S (2011) Improved synthesis of bulk metallic glasses by current-assisted copper mould casting. *Adv Eng Mater* 13: 38–42.
26. Amiya K, Inoue A (2000) Thermal stability and mechanical properties of Mg-Y-Cu-M (M = Ag, Pd) bulk amorphous alloys. *Mater Trans* 41: 1460–1462.
27. Nowosielski R, Babilas R (2011) Fe-based bulk metallic glasses prepared by centrifugal casting method. *J Achievements Mater Manuf Eng* 48: 153–160.
28. Wyslocki JJ, Pawlik P (2010) Arc-plasma spraying and suction casting methods in magnetic materials manufacturing. *J Achievements Mater Manuf Eng* 43: 463–468.
29. Figueroa IA, Caroll PA (2007) Davies HA Preparation of Cu-based bulk metallic glasses by suction casting. *Solidiication Processing 07 Proceedings of the 5th Decennial International Conference* on Solidification Processing, Sheffield, UK.
30. Yufeng S, Nobuhiro T, Shiro K (2007) Fabrication of bulk metallic glass sheet in Cu-47 at% Zr alloys by ARB and heat treatment. *Mater Tran*s 48: 1605–1609.
31. Lee MH, Lee KS, Das J (2010) Improved plasticity of bulk metallic glass upon cold rolling. *Scripta Mater* 62: 678–681.
32. Rizzi P, Habib A, Castellero A (2013) Ductility and toughness of cold-rolled metallic glasses. *Intermetallics* 33: 38–43.
33. Haruyama O, Kisara K, Yamashita A (2013) Characterisation of free volume in cold-rolled $Zr_{55}Cu_{30}Ni_5Al_{10}$ bulk metallic glasses. *Acta Mater* 61: 3224–3232.
34. Futterer H, Wernhardt R, Pelzl J (1983) Splat cooling device for preparation of metallic glasses in inert gases. *J Non-Cryst Solids* 56: 435–438.

35. Budhani RC, Goel TC, Chopra KL (1982) Melt-Spining technique for preparation of metallic glass. *Bull Mater Sci* 4: 549–561.
36. Xu M, Ye Y, Morris JR (2006) Influence of Pd on formation of amorphous and quasicrystal phases in rapidly quenched $Zr_2Cu_{(1-x)}Pd_x$. *Philos Mag* 86: 389–395
37. Limin W, Ma L, Inoue A (2003) Nanocrystal reinforced $Hf_{60}Ti_{15}Ni_5Cu_{10}$ metallic glass by melt spinning. J Alloy Compd 352: 265–269.
38. Schroers J, Quoc P, Amit D (2007) Thermoplastic forming of bulk metallic glass-A technology for MEMS and microstructure fabrication. *J Microelectromech S* 16: 240–247.
39. Ye JC, Chu JP, Chen YC (2012) Hardness, yield strength and plastic flow in thin film metallic-glass. *J Appl Phys* 112: 053516-053516-9.
40. Wei B-H, Chu C-W, Huang C-H, et al. (2013) Characteristic studies on Zr-based metallic glass thin film on antibacterial capability fabricated by magnetron sputtering process. *Bio Eng Res* 3: 48–53.
41. Liu Y, Liu J, Sohn S (2015) Metallic glass nanostructures of tunable shape and composition. *Nat commun* 6.
42. Santanu D, Santos-Ortiz R, Harpreet S (2016) Electromechanical behavior of pulsed laser deposited platinum-based metallic glass thin films. *Physica Status Solidi* 213: 399–404.
43. Wu X, Chen F, Zhang N, et al. (2016) Silver-Copper metallic glass electrocatalyst with high activity and stability comparable to Pt/C for Zinc-air batteries. *J Mater Chem A* 4: 3527–3537.
44. Nagar S (2012) Multifunctional magnetic materials prepared by pulsed laser deposition. Doctoral dissertation. Department of material Science and Engineering, School of Industrial Engineering and Management, Royal Institute of technology ,Stockholm
45. Saraf BM, Soodeh ZS (2013) Feasibility of Ti-based metallic glass coating in biomedical applications. *Proceedings of 20th Iranian Conference on Biomedical Engineering (ICBME 2013)*, 18–20 December, University of Tehran, Tehran, Iran.
46. Ningshen S, Kamachi MU, Krishnan R (2011) Corrosion behavior of Zr-based metallic glass coating on type 304L stainless steel by pulsed laser deposition. *Surf Coat Tech* 205: 3961–3966.
47. Dapeng J (2010) Metal thin film growth on multi metallic surfaces: From quaternary metallic glass to binary crystal. Iowa State university. Graduate Theses.
48. Pookat G, Thomas H, Thomas S (2013) Evolution of structural and magnetic properties of Co-Fe based metallic glass thin films with thermal annealing. *Surf Coat Tech* 236: 246–251.
49. Thomas S, Mathew J, Radhakrishnan P, et al. (2010) Metglas thin film based magnetostrictive transducers for use in long period fibre grating sensors. *Sensor Actuat A-Phys* 161: 83–90.
50. Chu JP, Lin CT, Mahalingam T (2004) Annealing induced full amorphisation in a multicomponent metallic film. *Phys Rev B* 69: 113410-1-4.
51. Chu JP, Wang C-Y, Chen LJ, et al. (2011) Annealing induced amorphisation in a sputtered glass forming film: In-situ transmission electron microscopy observation. *Surf Coat Tech* 205: 2914–2918.
52. Lin H-K, Lee C-J, Hu T-T, et al. (2012) Pulsed laser micromachining of Mg-Cu-Gd bulk metallic glass. *Opt Laser Eng* 50: 883–886.
53. Williams E, Brousseau EB (2016) Nanosecond laser processing of $Zr_{41.2}Ti_{13.8}Cu_{12.5}Ni_{10}Be_{22.5}$ with single pulses. *J Mater Process Tech* 232: 34–42.
54. Cheung TL, Shek CH (2008) Surface characteristics of nitrogen and argon plasma immersion ion implantation of Cu-Zr-Al bulk metallic alloy. *Rev Adv Mater Sci* 18: 112–120.

55. Huang H-H, Huang H-M, Lin M-C, et al. (2014) Enhancing the bio-corossion resistance of Ni-free ZrCuFeAl bulk metallic glass through nitrogen plasma immersion ion implantation. *J Alloy Compd* 615: S660–S665.
56. Tam CY, Shek CH (2007) Improved oxidation resistance of $Cu_{60}Zr_{30}Ti_{10}$ BMG with plasma immersion ion implantation. *J Non-Cryst Solids* 353: 3590–3595.
57. Qiu SB, Yao KF (2008) Novel application of the electrodeposition on bulk metallic glasses. *Appl Surf Sci* 255: 3454–3458.
58. Meng M, Gao Z, Ren L, et al. (2014). Improved plasticity of bulk metallic glasses by electrodeposition. *Mater Sci Eng A* 615: 240–246.
59. Turnbull D (1969) Under what conditions can a glass be formed. *Contemp Phys* 10: 473-488.
60. Inoue A, Koshiba H, Zhang T (1998) Wide supercooled liquid region and soft magnetic properties of $Fe_{56}Co_7Ni_7Zr_{0–10}Nb$ (or Ta)$_{0–10}B_{20}$ amorphous alloys. *J Appl Phys* 83: 1967–1974
61. Lu ZP, Liu CT (2002) A new glass forming ability criterion for bulk metallic glasses. *J Acta Mater* 50: 3501–3512.
62. Ji X, Ye P (2009) A thermodynamic approach to assess glass-forming ability of bulk metallic glasses. *Trans Nonferrous Met Soc China* 19: 1271–1279.
63. Thompson CV, Spaepen F (1979) On the approximation of the free energy change of crystallization. *Acta Metall* 27: 1855–1859.
64. Mondal K, Murty BS (2005) On the parameters to assess the glass forming ability of liquids. *J Non-Cryst Solids* 351: 1366–1371.
65. Ashmi TP, Arun P (2013) Study of glass transition kinetics for $Co_{66}Si_{12}B_{16}Fe_4Mo_2$ metallic glass. *Int J Mod Phys: Conference series* 22: 321–326.
66. Lafi OA, Imran MMA (2011) Compositional dependence of thermal stability, glass forming ability and fragility index in some Se-Te-Sn glasses. *J Alloys Compd* 509: 5090–5094.
67. Mukherjee S, Schroers J, Zhou Z (2004) Viscosity and specific volume of bulk metallic glass-forming alloys and their correlation with glass forming ability. *Acta Mater* 52: 3689–3695.
68. Daniel BM, Takeshi E, Katharine MF (2007). Structural aspects of Metallic Glasses. *Mater Res soc Bulletin* 32: 629–634.
69. Qin F, Wang X, Xie G, et al. (2007) Microstructure and corrosion resistance of Ti-Zr-Cu-Pd-Sn glassy and nanocrystalline alloys. *Mater Trans* 48: 167–170.
70. Laws KJ, Miracle DB, Ferry M (2015) A predictive structural model for bulk metallic glasses. *Nat Commun* 6: 1–10.
71. Sopu D, Albe K (2015) Influence of grain size and composition, topology and excess free volume on the deformation behavior of Cu-Zrnanoglasses. *Beilstein J Nanotech* 6: 537–545.
72. Daniel BM (2004) A structural model for metallic glasses. *Nat Mater* 3: 697–702.
73. Wang K, Fujita T, Chen MW (2007) Electrical conductivity of a bulk metallic glass composite. *Appl Phys Lett* 91: 154101-1-154101-3.
74. Umetsu R Y, Tu R, Goto T (2012) Thermal and electrical transport properties of Zr-Based bulk metallic glassy alloys with high glass – forming ability. *Mater Trans* 53: 1721–1725.
75. Dmitri VL, Larissa VL, Alexander YC (2013) Mechanical properties and deformation behavior of bulk metallic glasses. *Metals* 3: 1–22.
76. Zhang QS, Zhang W, Xie G, et al. (2010) Stable flowing of localised shear bands in soft bulk metallic glass. Acta Materialia 58: 904-909.
77. Chen HS (1973) Plastic flow in metallic glasses under compression. *Scr Metar* 7: 931–935.

78. Yu HB, Wang WH, Zhang JL (2009) Statistics analysis of the mechanical behavior of bulk metallic glasses. *Adv Eng Mater* 11: 370–375.
79. Daniel P, Yokoyama Y, Fujita K (2009) Correlation between structural relaxation and shear transformation zone volume of a bulk metallic glass. *Appl Phys Lett* 95: 141909-141909-3.
80. Louzguine DV, Kato H, Inoue A (2004) High-strength Cu-based cystal-glassy composite with enhanced ductility. *Appl Phys Lett* 84: 1088–1089.
81. Das J, Tang MB, Kim KB (2005) Work-hardenable ductile bulk metallic glass. *Phys Rev Lett* 94: 205501-1-205501-4.
82. Hajlaoui K, Yavari AR, LeMoulec A (2007) Plasticity induced by nanoparticle dispersions in bulk metallic glasses. *J Non-Cryst Solids* 353: 327–331.
83. Saida J, Kato H, Setyawan ADH (2005) Characterisation and properties of nanocrystal-forming Zr-based bulk metallic glasses. *Rev Adv Sci* 10: 34–38.
84. Coddet P, Sanchette F, Rousset JC (2012) On the elastic modulus and hardness of co-sputtered Zr-Cu-(N) thin metal glass film. *Surf Coat Tech* 206: 3567–3571.
85. Madoka O, Kyoko N, Ryuji T (2005) Tungsten-based metallic glasses with high crystallisation temperature, high modulus and high hardness. *Mater Trans* 46: 48–53.
86. Inoue A (2000) Stabilization of metallic supercooled liquid and bulk amorphous alloys. *Acta Mater* 48: 279–306.
87. Ye JC, Lu J, Yang Y, et al. (2010) Extraction of bulk metallic glass yield strengths using tapered micropillars in micro compression experiments. *Intermetallics* 18: 385–393.
88. Chou HS, Huang JC, Chang LW (2008) Structural relaxation and nanoindentation response in Zr-Cu-Ti amorphous thin films. *Appl Phys Lett* 93: 191901-1-191901-3.
89. Chou HS, Huang JC, Chang LW (2010) Mechanical properties of ZrCuTi thin film metallic glass with high content of immiscible tantalum. *Surf Coat Tech* 205: 587–590.
90. Johnson WL, Samwer K (2005) A universal criterion for plastic yielding of metallic glasses with a $(T/T_g)^{2/3}$ temperature dependence. *Phys Rev Lett* 95: 195501.
91. Blau PJ (2001) Friction and wear of Zr-based amorphous metal alloy under dry and lubricated conditions. *Wear* 250: 431–434.
92. Fu XY, Kasai T, Falk ML (2001) Sliding behavior of metallic glass – Part I. Experimental Investigations. *Wear* 250: 409–419.
93. Zeynep P, Mustafa B, Albert JS (2008) Sliding tribological characteristics of Zr-based bulk metallic glass. *Intermetallics* 16: 34–41.
94. Tam CY, Shek CH (2004) Abrasive wear of $Cu_{60}Zr_{30}Ti_{10}$ bulk metallic glass. *Mater Sci Eng A* 384: 138–142.
95. Prakash B (2005) Abrasive behavior of Fe, Co and Ni based metallic glasses. *Wear* 258: 217–224.
96. Bhushan B (2002) *Introduction to tribology*. John Wiley and Sons.
97. Jang B-T, Yi S-H, Kim S-S (2010) Tribological behavior of Fe-based bulk metallic glass. *J Mech Sci Technol* 24: 89–92.
98. Liu FX, Yang FQ, Gao YF (2009) Micro-scratch study of a magnetron-sputtered Zr-based metallic-glass film. *Surf Coat Tech 203*: 3480–3484.
99. Chunling Q, Katsuhiko A, Tao Z (2003) Corrosion behavior of Cu-Zr-Ti-Nb bulk glassy alloys. *Mater Trans* 4: 749–753.

100. Qin F, Yoshimura M, Wang X, et al. (2007) Corrosion behavior of a Ti-based bulk metallic glass and its crystalline alloys. *Mater Trans* 48: 1855–1858.
101. Vincent S, Khan AF, Murty BS (2013) Corrosion characterization on melt spun $Cu_{60}Zr_{20}Ti_{20}$ metallic glass: An experimental case study. *J Non-Cryst Solids* 379: 48–53.
102. Chen L-T, Lee J-W, Yang Y-C, et al. (2014) Microstructure, mechanical and anti-corrosion property evaluation of iron-based thin film metallic glasses. *Surf Coat Tech* 260: 46–55.
103. Inoue A, Shinohara Y, Gook JS (1995) Thermal and magnetic properties of bulk Fe-based glassy alloys prepared by copper mold casting. *Mater Trans* 36: 1427-1433.
104. Inoue A, Zhang T, Zhang W, et al. (1996) Bulk Nd-Fe-Al amorphous alloys with hard magnetic properties. *Mater Trans* 37: 99-108.
105. Boll R, Weichmagnetische W, GmbH VAC (1990) Siemens AG Berlin und München, Germany.
106. Chu JP, Lo CT, Fang YK, et al. (2006) On annealing-induced amorphisation and anisotropy in a ferromagnetic Fe-based film: a magnetic and property study. *Appl Phys Lett* 88: 012510-1-012510-3.
107. Wahyu D, Jinn PC, Berhanu TK (2015) Thin film metallic glasses in optoelectronic, magnetic and electronic applications: A recent update. *Curr Opin Solid State Mater Sci* 19: 95–106.
108. Kim H, Gilmore CM, Pique A (1999) Electrical, optical and structural properties of indium-tin-oxide thin films for organic light-emitting devices. *J Appl Phys* 86: 6451–6461.
109. Hu TT, Hsu J, Huang JC (2012) Correlation between reflectivity and resistivity in multi component metallic systems. *Appl Phys Lett* 101: 011902-1-011902-4.
110. Chen H-W, Hsu K-C, Chan Y-C, et al. (2014) Antimicrobial properties of Zr-Cu-Al-Ag thin film metallic glass. *Thin Solid Films* 561: 98–101.
111. Weissman Z, Berdicevsky I, Cavari BZ (2000) The high copper tolerance of Candida albicans is mediated by a P-type ATPase. *P Nati Acad Sci USA* 28: 3520–3525.
112. Chu JP, Tz-Yah L, Chia-Lin L (2014) Fabrication and characterisations of thin film metallic glasses: Antibacterial property and durability study for medical application. *Thin Solid Films* 561: 102–107
113. Chu YY, Lin YS, Chang CM (2014) Promising antimicrobial capability of thin film metallic glasses. *Mater Sci Eng C* 36: 221–225.
114. Sharma P, Kaushik N, Kimura H (2007) Nano-fabrication with metallic glass – An exotic material for nano-electromechanical systems. *Nanotechnology* 18: 035302-1-035302-6.
115. Trukenmuller R, Giselbrecht S, Rivron N (2011) Thermoforming of film-based biomedical microdevices. *Adv Mater* 23: 1311–1329.
116. Kaushik N, Sharma P, Ahadian S (2014) Metallic glass thin films for potential biomedical applications. *J Biomed Mater Res Part B* 102: 1544–1552.
117. Felix G, Klaus V, Wei-Shan W (2015) Towards MEMS loudspeaker fabrication by using metallic glass thin films. Fraunhofer Institute for Electronic Nano Systems ENAS. Available from: http://www.enas.fraunhofer.de/content/-
118. Seiichi H, Junpei S, Akira S (2005) Thin film metallic glasses as new MEMS materials. *IEEE International Conference on Micro Electro Mechanical Systems*.
119. Junpei S, Seiichi H (2015) Characteristics of Ti-Ni-Zr thin film metallic glasses/thin film shape memory alloys for micro actuators with three dimensional structures. *Int J Autom Tech* 9: 662–667.

120. Susumu K, Shin-ichi Y, Hisamichi K (2010) Composition control of Pd-Cu-Si metallic glassy alloys for thin film hydrogen sensor. *Mater Trans* 51: 2133–2138.
121. Ishida M, Takeda H, Watanabe D (2004) Fillability and imprintability of high strength Ni-based bulk metallic glass prepared by the precision Die-casting technique. *Mater Trans* 45: 1239–1244.
122. Inoue A, Wang XM, Zhang W (2008) Developments and applications of bulk metallic glasses. *Rev Adv Mater Sci* 18: 1–9.

AIMS Press